Master-Thesis

Investigation of the gas-liquid mass transfer in trickle bed reactors

Institute of

Chemical, Environmental and Bioscience Engineering

submitted at TU Wien

under the supervision of

Ass.Prof. Dipl.-Ing. Dr.techn. Michael Harasek

Projektass. Dipl.-Ing. Christian Jordan

Projektass. Bahram Haddadi Sisakht MSc.

by

Maximilian Reindl

Mat. Nr.: 01225859

Vienna, November 23, 2018

Affidavit

I confirm, that going to press of this thesis needs the confirmation of the examination committee.

I, Maximilian Reindl, declare in lieu of oath

1 that I wrote this thesis and performed the associated research myself, using only literature cited in this volume. If text passages from sources are used literally, they are marked as such.

2 that this work is original and has not been submitted elsewhere for any examination nor is it currently under consideration for a thesis elsewhere.

Vienna, November 23, 2018 _____

Danksagung

Ich möchte mich sehr herzlich bei Michael Harasek für die Möglichkeit bedanken diese Diplomarbeit in seiner Forschungsgruppe zu absolvieren. Im selben Atemzug müssen auch Christian Jordan und Bahram Haddadi erwähnt werden, die mir bei jeder Frage zur Seite standen und mich überall unterstützten. Das Studium war aber nicht nur von Arbeit geprägt. Auch Freundschaften entstanden. Diese Freunde haben mich während meiner ganzen Studienzeit begleitet. Vielen Dank an meine Kollegen. Auch meine Eltern müssen erwähnt werden. Diese wussten zwar oft nicht was ich mache, standen mir aber trotzdem immer zur Seite. Vielen Dank auch an Christine und Klaus Simon. Zu guter letzt muss auch Carina gedankt werden, die es nicht immer leicht mit mir hatte und trotzdem zu mir gehalten hat. Vielen Dank!

Zusammenfassung

Unter Absorption versteht man die Aufnahme einer Komponente aus der Gasphase in einer Flüssigphase. Absorptionsprozesse sind keine neue Erfindung der Menschheit, in der Natur finden Absorptionsprozesse schon seit Anbeginn der Zeit statt. Der Mensch hat sich dieses Phänomen zu Nutzen gemacht um neue Produkte zu erstellen , die Wirtschaftlichkeit von Produktionsverfahren zu verbessern und den im Zuge der Produktion verursachten Schaden an der Natur wieder zu reduzieren. So entstanden über die Zeit viele verschiedene Arten von Absorbern, welche von diversen Vor- und Nachteilen begleitet werden. In dieser Arbeit wird auf Rieselbettreaktoren eingegangen. Hierbei strömen ein oder mehrere Fluide durch eine feste Packung.

Da der Stoffaustausch zwischen den verschiedenen Phasen vor allem von den Strömungsbedingungen in der Kolonne abhängt muss auf diese besonderes Augenmerk gerichtet werden. Aus diesem Grund wurde auf die Erforschung des hydrodynamische Verhalten der Prozesse schon viel Wert gelegt.

Aufgabenstellung dieser Arbeit war, Daten zur Validierung eines Strömungssimulationsprogrammes zur Berechnung der Vorgänge während eines Absorptionsprozesses experimentell zu ermitteln. Zu diesem Zweck wurde eine bestehende Labor-Blasensäule revitalisiert, umgebaut und als Rieselbettreaktor in Betrieb genommen. Der Korpus wurde mit inerten, kugelförmigem nicht porösem Bettmaterial gefüllt. Um das Verhalten der flüssigen Phase und den Stoffübergang analysieren zu können wurde die Kolonne mit verschiedenen Flüssigkeitsberieselungsdichten und unterschiedlichen Gas-flussraten betrieben, die im Gegenstrom aufgegeben wurden. Als Medien für diese Versuche dienten Leitungswasser und Luft. Als wesentliche Untersuchungsparameter wurde der Hold-Up des Wassers in der Packung und der Sauerstoffübergang zwischen beiden Phasen bei den diversen Betriebsbedingungen definiert.

Zur Bestimmung der Flüssigkeitsverweilzeit un der axialen Rückvermischung des Reaktores zu ermitteln, wurde ein Tracerverfahren verwendet. Mittels eienr konzentrierten Salzlösung wurde ein Puls am Kolonnenkopf aufgegeben, die Pulsantwort wurde am Boden der Kolonne mittels Leitfähigkeitssonden gemessen. Zur Ermittlung des Sauerstoff-Phasenüberganges wurden zur Erstellung einer Stoffmengenbilanz je zwei Sauerstoffsensoren für die Flüssig- und zwei für die Gasphase zur Datenerfassung herangezogen.

Die analysierten Werte wurden mit bestehenden Korrelationen verglichen. Um die axiale Dispersion für die flüssige Phase zu bestimmen wurde die Verteilungsfunktion von Levenspiel ausgewählt. Diese wurde benutzt um charakteristische Parameter wie die mittlere Verweilzeit und den Dispersionskoeffizienten zu errechnen. Die Bodenstein- und die Pecletzahl wurden als Kennzahlen herangezogen um die Ergebnisse mit den bestehenden Korrelationen vergleichen zu können. Die gefundenen Näherungen ergeben für bestimmte Bereiche gute Vorhersagen.

Durch die Entwicklung von leistungsfähigerer Hardware und den damit steigenden Rechenkapazität erhählt die Berechnung von fluiddynamischen Problemen, mittels Computer, immer mehr Aufmerksamkeit. Diese Arbeit hat sich neben der durchgeführten Experimente auch mit der CFD (Computational Fuild Dynamics)-Simulation beschäftigt. Die Kugelpackung wurde mit Hilfe der diskreten Elemente Methode (DEM) erstellt. Die Simulation wurde mit OpenFOAM durchgeführt. Die Ergebnisse dieser numerischen Berechnung stellt die Grundlage für weitere Arbeiten dar.

Abstract

Absorption is the ability of a component in the gas phase to dissolve into the liquid phase. Since begin of the time absorption is a natural phenomenon. This process is used by the humanity to build new products, increase the productivity and decrease the environmental pollution. Over the time different kind of absorber have been invented. Each type of this absorbers have different advantages and disadvantages. In this thesis the behavior of a trickle bed reactor is investigated. In this kind of absorber one or more fluid phases flow threw a fixed packed bed. The mass transfer in this reactors is dependent on the flow conditions of the fluid phases. The important hydrodynamic conditions of the trickle bed are investigated in this thesis.

The task of this work was to evaluate data of the absorption process to validate the simulations of a computational simulation. For this investigations an existing laboratory bubble column is revitalized and rebuild to a trickle bed reactor. For the fixed bed spherical particles are used. These particles have a non porous and a non inert character. To investigate the behavior of the liquid phase in the trickle bed the experiments are done with different liquid- and gas flow rates. For the experiments regular tab water and ambient air have been used. The hold-up of the liquid phase and the oxygen mass transfer in the trickle bed have been investigated for different flow conditions of the phases. For the hold-up experiments a tracer method was used. A salt solution was injected at the top of the column and the response was detected at the bottom of the trickle bed by a conductivity sensor. The mass transfer experiments were recorded with two oxygen sensors for the liquid and two oxygen senors for the gas phase. The results of the recorded data are compared with existing correlations.

To determine the axial dispersion of the liquid phase the approach of Levenspiel is used. This distribution function is used to evaluate the average residence time and the axial dispersion coefficient. To compare the results of the used setup with other cases the Bodenstein- and Peclet number are used. This correlations deliver good approximations for certain flow conditions.

The development of more powerful hardware and the increasing computing capacity, more attention on the calculation of fluid dynamic problems by computer can be paid. Next to the evaluation of the experimental data this thesis uses computational fluid dynamics (CFD) to simulate this task. The sphere packing for the simulation is created by a discrete element method (DEM). For the numerical calculation the software OpenFOAM is used. This simulation is the base for further investigations.

Contents

List of Figures

List of Tables

Chapter 1.

Motivation

The chemical absorption process makes it possible to assimilate or dissolve substances in the liquid or gas phase. Since the environmental awareness of the people is rising absorbers are more important than before. Used as gas scrubbers, pollutants can be washed out of exhaust gases. For a better economic efficiency reusable material can be separated from the exhaust gas. For a better efficiency of theses absorption columns the following parameters have to be considered. Chemical reactions, the contact time between both phases and the surface of the substance transfer are important values which have to be considered. Industries are aware of the importance of these parameters. Therefore many studies have already been conducted for hydrodynamic properties and the involved mass transfer in these process units. One part of this field are fixed bed reactors. By adding packing material these operation units provide a bigger process surface for the exchange between the different phases and chemical reactions. Some of these packings also have a catalytic character. The chemical effect of the catalytic packing material has already been well explored.

The flow down a trickle bed is not equal to a standard plug flow. Due to a back mixing of the liquid phase a longer residence time and a better mass transfer are provided. This deviation to the standard plug flow can be described with dimensionless numbers like the Peclet or Bodenstein number and it is dependent on the flow boundary conditions at the gas - and water inlet. The problem with most existing scientific approaches is their consideration of just one phase. Axial dispersion is often described for a single phase liquid flow threw the packing [Ram, 1966]. For different gas flow rates at constant water flow rates, the investigated calculations would remain at the same value. This conflicts with the hydrodynamic properties in the trickle bed at different air flow rates. The rising computational power favors the numerical modeling and solving by computational fluid dynamics (CFD). Investigations

using this tool have only been used for small parts or for two - dimensional problems, like the hydrodynamic behavior of the packing or the mass transfer in the packing [Atmakidis and Kenig, 2012] and [Gunjal et al., 2005]. Scientific literature describes the hydrodynamics but not the mass transfer. These approaches require less computational power than a big setup with all its details. The approach of determining hydrodynamic behavior and the associated mass transfer between the phases also can not be found in the current literature. However for many industries the mass transfer is very important for optimizing their processes in order to increase their yield and raise their profits. The industrial sector is aware of the necessity for evaluating and optimizing the mass transfer in the used units before they are being built.

The aim of this thesis is to remodel an existing experimental setup and adapt it in a way so it can be used for different tasks. This construction was originally built as a bubble column in 2008 by Michael Lukasser [Lukasser, 2008]. The plan was to use it as a fixed bed reactor with non-catalytic particles and to evaluate the behavior of the liquid phase at different air flow rates in the trickle bed. Also the oxygen transfer from the gas- to the liquid phase was observed and the boundary conditions of the setup are evaluated. With a simulation the results from the experiments could be compared to the numerical solution provided by the simulated model.

Chapter 2.

Theoretical Principles

2.1. Absorption

Absorption is a thermal separation process based on material exchange between a gas and a liquid phase. The mass transfer occurs during the contact time of the gas and the liquid phase. Physical forces and chemical compounds are limiting the solubility of the gas in a solvent. For this process the gas phase gets in contact with the liquid phase in an absorber. Dependent on the predominant binding forces between the chemical substances the optimum procedure has to be chosen. This provides two different kinds of absorption processes, the physical absorption and the chemical absorption.

2.1.1. Physical Absorption

During a physical absorption the absorptive is dissolved without changing the substance properties. The gas dissolves directly from the gas phase into the liquid phase, if there is a perfect physical solubility. The equilibrium of the dissolving component is described by the law of Henry. In equation 2.1 the index i is used for the absorbed species.

$$p_{\mathrm{i}} = H_{\mathrm{i}} \cdot x_{\mathrm{i}} \tag{2.1}$$

p_i describes the partial pressure and x_i the mole fraction of the component i in the liquid phase. H_i is the Henry constant of the species i.

With the law of Dalton the partial pressure can be evaluated. The total pressure p and the mole fraction y_i of the component i in the gas phase are used.

$$p_{\mathrm{i}} = y_{\mathrm{i}} \cdot p \tag{2.2}$$

The law of Raoult calculates the relation between the partial pressure and the temperature dependent, vapour saturation pressure p $_{\mathrm{o,i}}$ of the pure component i.

$$p_{\mathrm{i}} = p_{\mathrm{o,i}}(T) \cdot x_{\mathrm{i}} \tag{2.3}$$

With the two laws of Dalton (equation 2.2) and Raoult (equation 2.3) the connection of the mole fraction in the gas and the liquid phase can be calculated.

$$x_{\mathrm{i}} = y_{\mathrm{i}} \frac{p}{p_{\mathrm{o,i}}(T)} \tag{2.4}$$

For a nonideal solution the activity coefficient γ_i can be used to adjust the equation. This is a result of the different interactions between the molecules in different substances.

$$x_{\mathrm{i}} = y_{\mathrm{i}} \frac{p}{p_{\mathrm{o,i}}(T) \cdot \gamma_i} \tag{2.5}$$

The used activity coefficient is dependent on the concentration of the component i and the temperature.

The real dependency of the partial pressure of the mole fraction x_i in the liquid phase lies between the law of Raoult and Henry. These two laws describe the limits for high concentrations, $x_i \to 1$ and strongly diluted solutions $x_i \to 0$ as seen in figure 2.1.

By increasing the amount of the absorbed species in the gas phase and the total pressure, as well as decreasing the temperature the physical ability of dissolution in the liquid phase rises.

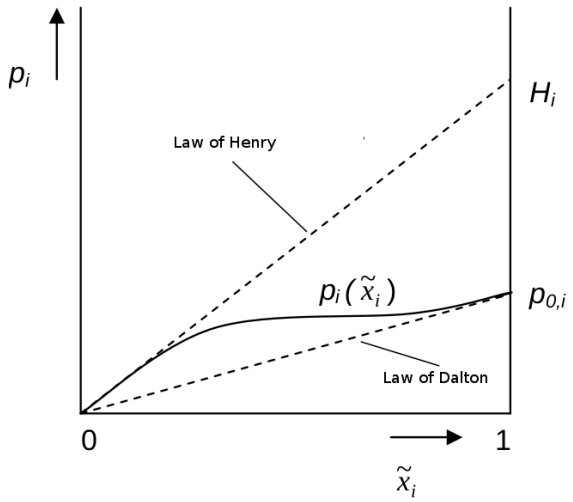

Figure 2.1.: Relevance of the liquid mole fraction for the partial pressure [Ohle, 2009]

2.1.2. Chemical Absorption

Chemical absorption starts with the physical bonding of the components by the van der Waals forces. In a second step a chemical reaction between the dissolved substance and the washing agent takes place in the liquid phase. The result is a non volatile product. The partial pressure p_i of the solute in the solution starts to increase when the component which reacts is almost consumed by the liquid phase. This behavior is illustrated in figure 2.2. This figure contrasts the changes in partial pressure during the physical and chemical absorption. The chemical equilibrium is described with the law of mass action.

$$\nu_A A + \nu_B B \leftrightarrow \nu_C C + \nu_D D \tag{2.6}$$

The equilibrium constant for the chemical reaction illustrates on which side of the equation the equilibrium takes place. For this stoichiometric coefficients, ν_i, and the substance mole fractions, x_i are used. This constant is dependent on temperature.

$$K(T) = \frac{{x_C}^{\nu_C} \cdot {x_D}^{\nu_D}}{{x_A}^{\nu_A} \cdot {x_B}^{\nu_B}} \tag{2.7}$$

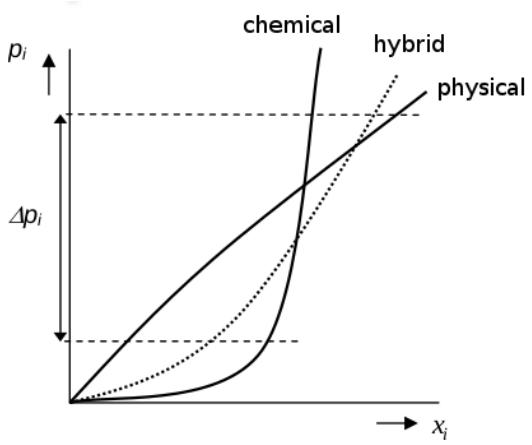

Figure 2.2.: Dependency of partial pressure on substance amount fraction [Ohle, 2009]

2.2. Mass Transfer

A mass transfer in an absorption column is characterized by the absorption process in two fluid phases, the liquid and the gas phase. The driving force for the mass transfer is the concentration difference of the species being transferred. The speed of the mass transfer is specified over the concentration gradient and the transfer resistance in the boundary layer. There are many different mathematical models that describe the mass transfer between two fluids. The problem with these models is that the actual hydrodynamic circumstances are not fully considered [Chmiel, 2011]. The next section illustrates the most common models and in figure 2.3 a quick overview of the mentioned theories can be seen.

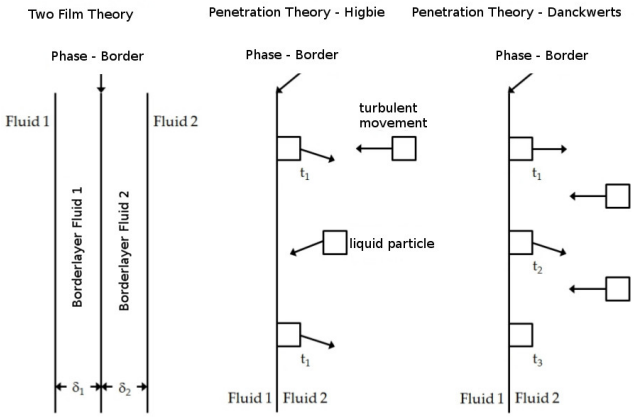

Figure 2.3.: Different models of mass transfer [Kemper, 2013]

2.2.1. Two Film Theory

One of the simplest forms to describe a mass transfer is the Two Film Theory which was invented by Lewis and Whitman [Kemper, 2013]. This theory requires a laminar fluid film on both boundary layers. In these layers the complete transfer resistance occurs. There is no exchange between the core of the phases and the thin laminar layer. The mass transfer is limited to the molecular diffusion.

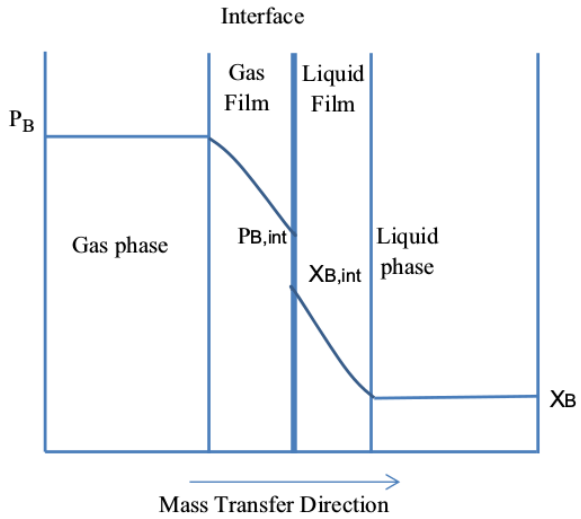

Figure 2.4.: Schematic Diagram of the Two Film Theory [Luo et al., 2014]

In figure 2.4 the concentration gradient of the specific transport mechanism is shown where P_B stands for the partial pressure of the gas phase and X_B for the mole fraction of the liquid phase. The Two Film Theory is a rather simplistic model which leads to some weaknesses. There is no reasonable way to predict that the rate of mass transfer is directly proportional to the molecular diffusivity. Also the thicknesses of the two laminar layers are hard to predict by experiment and the model requires a steady state mass transfer process [Luo et al., 2014]. A thermodynamic equilibrium exists on the boundary of the two phases.

$$p_{B,g} = p_B^* \tag{2.8}$$

$$X_{B,l} = X_B^* \tag{2.9}$$

Due to the proportionality of the mole fraction to the concentration, the equilibrium concentration can also be used to describe the boundary layer area.

$$c_{B,l} = c_B^* \tag{2.10}$$

Under this circumstance it is possible to simplify the model to linear concentration gradients in both boundary layers. The diffusion through the film can be described by the diffusion flux which is defined by the first diffusion equation according to Fick.

$$J_B = -D_B \frac{\Delta c_B}{\delta} \tag{2.11}$$

The mass transfer coefficient, β , is the ratio of the diffusion coefficent D_B and the thickness of the layer δ .

$$\beta_B = \frac{D_B}{\delta} \tag{2.12}$$

As in most cases the layer thickness is unknown, it is recommended to search for specifications in the relevant literature and estimate the thickness of the boundary layers. [Bähr and Stephan, 2006]

In case of an stationary processs the diffusion flux of a component (B) has to be the same on both sides of the boundary throughout the phase interface.

$$J_{Bg} = J_{Bl} = J_B \tag{2.13}$$

The law of Henry is valid in equilibrium conditions at our phase boundary.

$$p_B^* = H_B \cdot c_B^* \tag{2.14}$$

The H_B in this equation stands for Henry's constant and defines the proportionality of the concentration of the substance B, which is dissolved in the liquid phase, and the partial pressure of the gas above the water surface.

With the equations 2.15 and 2.16 the diffusion flux of the gas and the liquid phase can be calculated.

$$J_{B,g} = \frac{\beta_{B,g}}{R \cdot T}(p_{B,g} - p_B^*) \tag{2.15}$$

$$J_{B,l} = \beta_{B,l}(c_B^* - c_{B,l}) \tag{2.16}$$

2.2.2. Boundary Layer Theory

The boundary layer theory is similar to the Two Film Theory. In both models the mass transfer takes place in a thin layer at the boundary. The boundary layer theory accepts more variable parameters than the Two Film Theory. As well as the diffusive, a convective substance transfer take place. In contrast to the Two Film Theory the velocity and the concentration profiles are allowed to change in all directions and are not limited to the boundary layer (see 2.5). The limitation of this theory is, that the second derivation in the direction of x is much smaller then the one of the direction of y $\frac{\partial^2 c_A}{\partial x^2} << \frac{\partial^2 c_A}{\partial y^2}$.

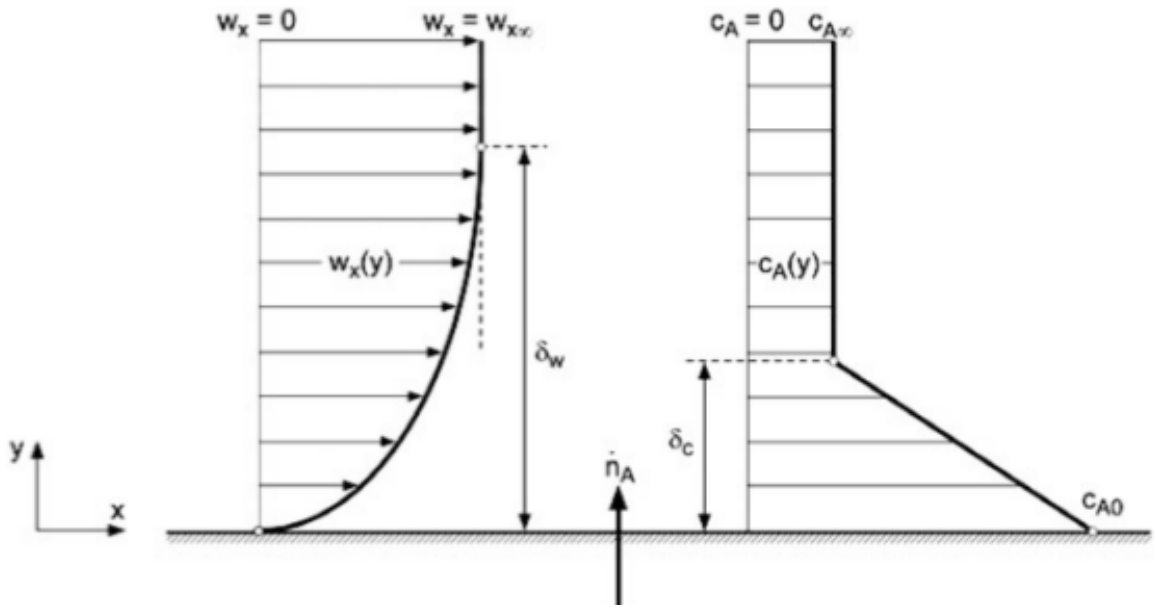

Figure 2.5.: Concentration and velocity profile on a overflowed surface [Kraume, 2012]

In this case there is a thin concentration boundary layer where the change of the concentration is big compared to other directions. Therefore it is only necessary to consider the diffusion in the direction of y. [Kraume, 2012]

2.2.3. Penetration Theory

Contrary to the two film theory, the Penetration Theory does not require a steady state. In many devices the time of contact between the liquid and the gas phase is very short. Nevertheless a mass transfer occurs during this time. A possible behavior of the contact zone can be seen in figure 2.6.

In case of a transient behavior a global mass transfer coefficient as in equation 2.12 is not useful for the Two Film Theory. Instead of this an average mass transfer coefficient should be defined.

$$\beta_{\mathrm{m}} = \frac{2}{\sqrt{\pi}} \sqrt{\frac{D}{t}} \tag{2.17}$$

In this equation β_m signifies the average mass transfer coefficient in the time from t=0 to t and D represents the diffusion coefficient between the two phases. In this case a constant contact time for each element is assumed [Higbie, 1935].

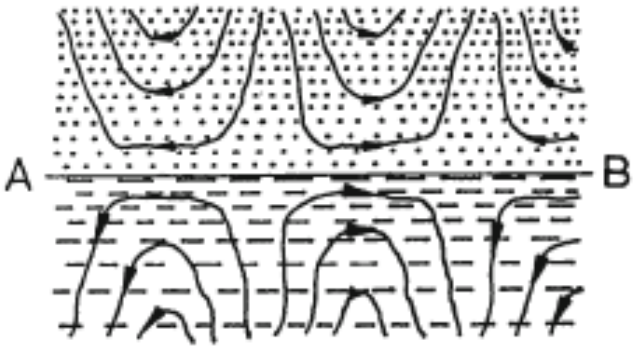

Figure 2.6.: Streamlines in the contact zone of two phases [Bähr and Stephan, 2006]

The transient mass transfer is described by the second diffusion equation by Fick.

$$\frac{\partial c_{\mathrm{i}}}{\partial t} = D_{\mathrm{i}} \cdot \frac{\partial^2}{\partial y^2} \tag{2.18}$$

Together with the first diffusion law of Fick the diffusion flux is described.

$$J_{i,l}(t) = \sqrt{\frac{D_{i,l}}{\pi \cdot t}} \cdot ({c_{i,l}}^{*} - c_{i,l}) \tag{2.19}$$

The contact time differs in each place. Danckwerts came up with a modification of the theory of Higbie. The residence time is used for describing such a case.

$$E(t) = s \cdot e^{-s\,t} \tag{2.20}$$

In this equation s stands for the proportion of the surface which gets renewed at each time step t. The average diffusion flux results in the equation 2.21

$$\overline{J}_i = s \cdot \int_0^{\infty} e^{-s\,t} \cdot J_i(t)dt = \sqrt{D_{i,l} \cdot s}({c_{i,l}}^{*} - c_{i,l}) \tag{2.21}$$

After a time period a fluid element is displaced from its place and gets replaced by a new element. This resulting in a turbulent boundary layer shown in figure 2.3 [Danckwerts, 1951].

The Penetration Theory also has deficits due to unknown parameters, like the passed time until a surface gets renewed or the contact time between the two phases.

2.3. Trickle-Bed Reactors

Trickle-bed reactors are used for reactions and substance transfer between at least two phases. One of the components is in the downward moving liquid phase, the other one is in the gas phase. The flow of the gas phase can be co- or counter current. The bed itself consist of solid filling material which provides a larger surface for the mass transfer. The packing material can have many different shapes and sizes. The choice of the used particles for the packing depends on the process. In order to be able to use the big surface the downward moving liquid should flow through the packing material in form of rivulets, films and droplets [Gianetto and Specchia, 1992]. The result of these fluid movements is a very low pressure loss over the bed and a high fluid dynamic limit.

In case of a counter current flow the gas is introduced to the bottom and removed at the top of the column. This can be seen in figure 2.7. The aim of this kind of process is to achieve a good phase distribution and the largest surface area for the mass transfer.

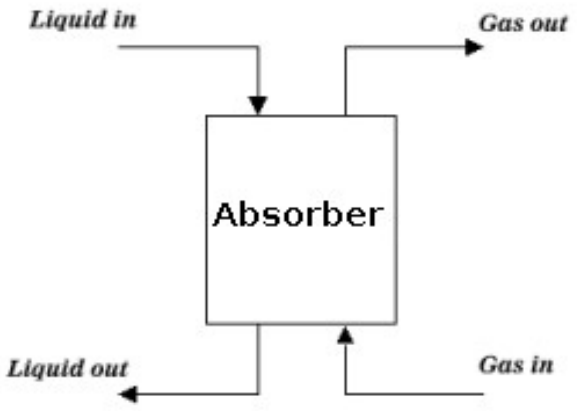

Figure 2.7.: Schematic picture of counter current flow in an absorber

Although a liquid flow in rivulets is desired, the building of streams should be avoided as streams cause a bad exploitation of the available surfaces and lead to a bad substance transfer.

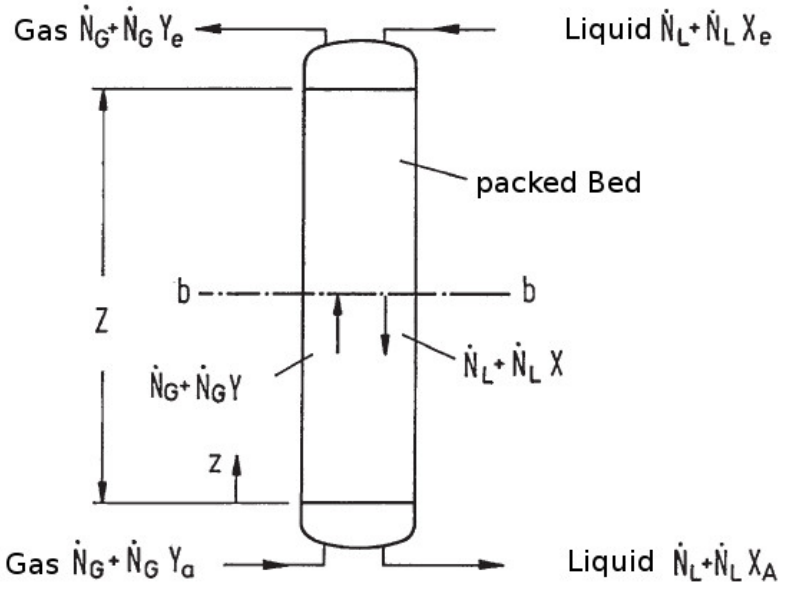

Figure 2.8.: Countercurrent absorber [Bähr and Stephan, 2006]

2.3.1. Quantitative balance and concentration profile over the trickle bed

The base for the design of an absorption column are the quantitative balances that describe the concentration of the different fluid flows.

In figure 2.8 an absorption column with a liquid downward flow and an upwards flowing gas is shown. The component A is being dissolved from the gas phase to the liquid phase. Both phases in this case are immiscible. The loading of the phases, X for the liquid and Y for the gas, are defined by the ratio of the amount of the substances for the component A and the total amount of the substance.

$$X_A = \frac{\dot{N}_{\mathrm{LA}}}{\dot{N}_{\mathrm{L}}} \tag{2.22}$$

$$Y_A = \frac{\dot{N}_{\mathrm{GA}}}{\dot{N}_{\mathrm{G}}} \tag{2.23}$$

The ratio between the amounts of substances results from the quantitative balance and is valid for steady state solutions. The indices a and e stand for the entrance (e) and the exit cross section (a) of the liquid phase.

$$\dot{N_L}X_e - \dot{N_G}Y_e - \dot{N_L}X_a + \dot{N_G}Y_a = 0 \tag{2.24}$$

For changes in the composition of the gas or the liquid phase a random balance boundary can be chosen. In this case the boundary b has been chosen.

$$\dot{N_L}X_e - \dot{N_G}Y_e - \dot{N_L}X + \dot{N_G}Y = 0 \tag{2.25}$$

$$Y = \frac{\dot{N_L}}{\dot{N_G}}X + (Y - \frac{\dot{N_L}}{\dot{N_G}}X_e) \tag{2.26}$$

This balances show that average gas loading and average liquid loading have a linear connection. So it is possible to set a correlation between those phases over the column. To get a local concentration profile in the absorber this approach cannot be used. In this case a

differential section has to be introduced. Through an integration of the concentration development the height of the column can be calculated. For this task the boundary between the two phases is a parameter commonly chosen.

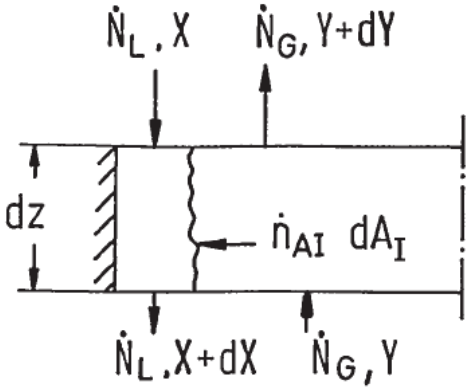

Figure 2.9.: Differential control volume [Bähr and Stephan, 2006]

In this case the phase boundary area, A_I, is obtained for the volume of the empty column, V_K, and the volume based boundary border, a^*.

$$a^* := \frac{A_I}{V_K} \tag{2.27}$$

Z describes the height of the column. So the Volume of the column, V_K, can be calculated as usual.

$$V_K = A_K Z \tag{2.28}$$

The two dimensional control volume, figure 2.9, has the distance dz and the length of the phase boundary dA_I. The transferred mass on this phase boundary is balanced as usual.

$$\dot{n_{\mathrm{AI}}} dA_I = \dot{n_{\mathrm{AI}}} a^* A_K dz \tag{2.29}$$

The substance A is transferred from the gas to the liquid phase. The quantity of the transferred substance from the gas phase must now be handled by liquid phase.

$$\dot{n_{\mathrm{Al}}} a^{*} A_K dz = -\dot{N_G} dY \tag{2.30}$$

With the mass transfer coefficient for the gas phase

$$k_G = \frac{\dot{n_{\mathrm{Al}}}}{y_{\mathrm{Am}} - y_{\mathrm{Aeq}}} \tag{2.31}$$

the differential height for a certain amount of transferred substance can be calculated. In equation 2.31 the index Am is defined by the integral average and Aeq stands for the equilibrium condition of the transferred substance. Under the circumstances of a small loading the molecular parts can be assumed $y_{\mathrm{Am}} = Y$ and $y_{\mathrm{Aeq}} = Y_{\mathrm{eq}}$

$$k_G (Y - Y_{\mathrm{eq}}) a^{*} A_K dz = -\dot{N_G} dY \tag{2.32}$$

$$dz = \frac{-\dot{N_G}}{k_G a^{*} A_K (Y - Y_{\mathrm{eq}})} dY \tag{2.33}$$

The needed height of the column can be calculated by an integral over the loading. In many cases this integral can be solved numerically. The equilibrium condition changes throughout in the column and is often described by complex functions [Bähr and Stephan, 2006].

2.3.2. Hydrodynamics

The knowledge of hydrodynamics is the basis needed to evaluate reactor properties. Properties of interest are the physical and chemical interactions like the pressure drop, the holdup, the heat and mass transfer. It is difficult to predict the hydrodynamics in a packed bed. A defined fluid flow at the top trickle bed is not sufficient to provide any information of the velocity distribution or the thickness of the liquid layer on the particles in the packed bed. The inconsistent distribution of the filling material leads to geometrically uncertain liquid streams throughout the bed. Another big issue is the time dependency of the surface layer of the fluid. Therefore it is only possible to make macroscopic assumptions [Kraume, 2012]. Aside from standard parameters like the physical characteristics of the gas and liquid, or the properties of the bed (porosity, the shape of the pellets), the conditions for the upwards and downwards flow are important.

Flow Regime

The flow conditions in a trickle bed are complicated. The three phases, liquid, gas and solid, influence each other. This makes it more complex than a single phase flow. In case of a trickle bed a cocurrent flow between the gas and the liquid phase take place. The dominant flow regime depends on many factors as for instance the flow rates of gas and water or the shape and the size of the particles. Four different flow regimes of trickle bed reactors are mentioned in the literature:

- Trickle flow regime
- Pulse flow regime
- Spray flow regime
- Bubbly flow regime

In case of a fixed geometry and packing the flow regimes can be achieved by varying the flow rates of the gas and the liquid [Ramachandran and Chaudhari, 1983].

In figure 2.10 the four different flow regimes are shown. The spheres illustrate the particles, the gas phase is white and the liquid phase is grey.

If the gas flow rate as well as the liquid flow rate are low the liquid flows down in form of a film flow over the solid particles. In this flow regime a continuous or at least a semicontinuous flow where all particles are wetted appears (2.10(a)). If the gas flow increases the interaction of the surfaces between the gas and the solid phase increases as the suspended droplets in the gas phase add to the liquid film on the particles (2.10(b)). When the gas flow rate increases more, a spray regime is achieved. In this case the whole liquid phase is suspended in droplets (2.10(c)). On the other hand if the liquid flow rate rises the gas gets dispersed in the water phase. This state is called bubbly flow regime (2.10(d)) [Gunjal et al., 2005].

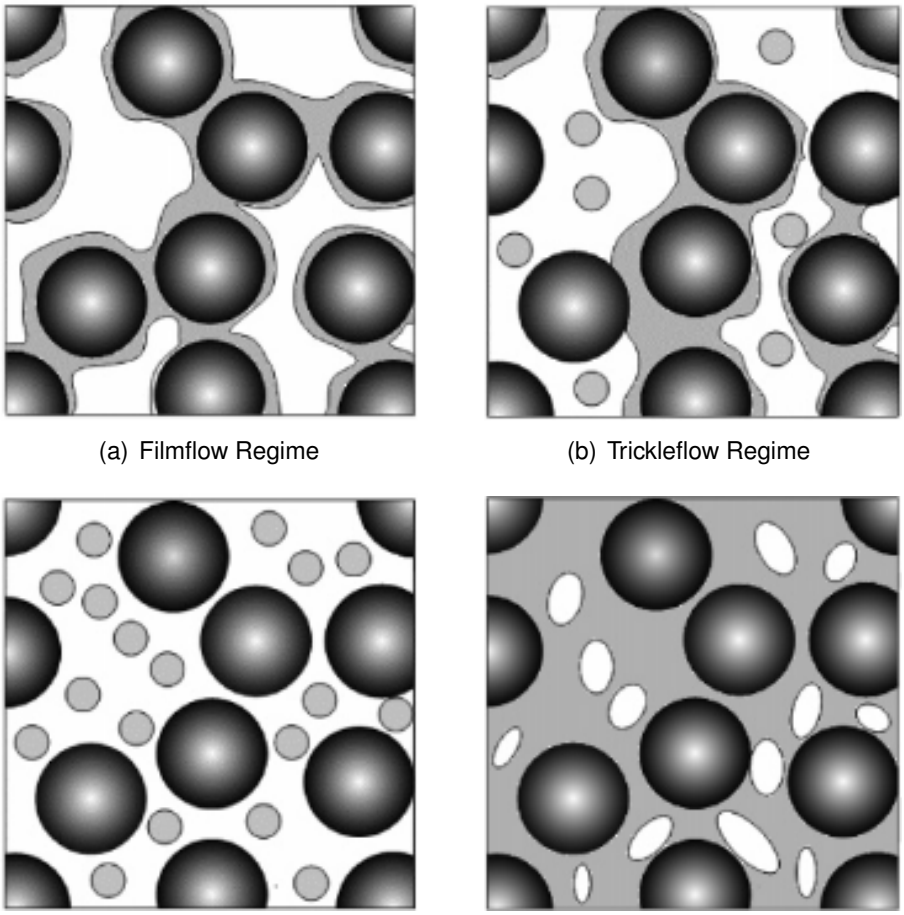

(a) Filmflow Regime (b) Trickleflow Regime

(c) Sprayflow Regime (d) Bubblyflow Regime

Figure 2.10.: Flow Regimes depending on gas- and waterflow rate [Gunjal et al., 2005]

These different flow regimes influence transport processes like the heat or the mass transfer on the boundary of the phases. The knowledge of the prevailing flow conditions is an important parameter for scale up or scale down processes. To run a trickle bed in an economical way the right flow regime has to be chosen. For the relevant industries it is quite common to operate such reactors between the trickle- and the pulse flow regimes. Under these conditions an increasing mass transfer and catalyst utilization occurs. The important parameters for the estimation of the flow regime in a trickle bed are the size and the shape of the particles, the porosity of the bed and the properties of the gas-liquid phases such as the viscosity, density, surface tension or contact angles. Also the operating conditions, especially the superficial velocities of the gas- and the liquid phase, have an influence on the dominant regime [Gunjal et al., 2005].

In figure 2.11 a flow map of a trickle-bed reactor is shown. In this picture G stands for the gas- and L for the liquid superficial mass flux density [kg/m^{2}s]. In this case λ stands for a gas phase parameter and ψ for the liquid phase parameter of the trickle-bed. The definition of this parameter can be seen in equation 2.34 and 2.35

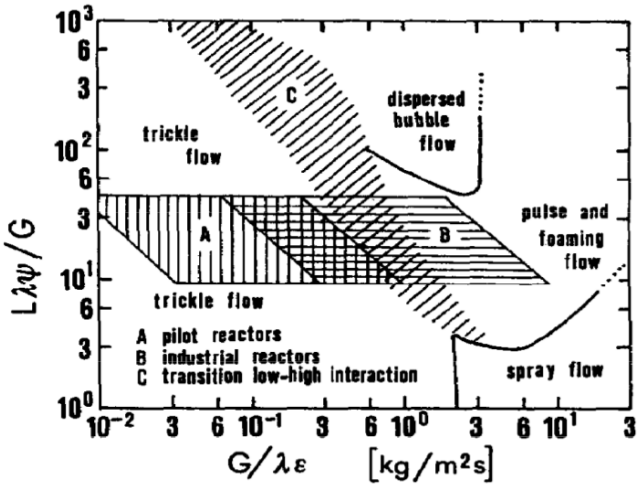

Figure 2.11.: Flow Map of a Trickle Bed Reactor [Gianetto and Specchia, 1992]

$$\lambda = \left(\frac{\rho_g \cdot \rho_l}{\rho_{\text{air}} \cdot \rho_{\text{water}}}\right)^{0.5} \tag{2.34}$$

$$\psi = \frac{\sigma_W}{\sigma_L}\left[\frac{\mu_L}{\mu_W}\left(\frac{\rho_W}{\rho_L}\right)^2\right]^{1/3} \tag{2.35}$$

The properties of air and water are evaluated at standard conditions.

For many different kinds of hydrodynamic regimes experiments have been examined. The results of many authors have been summed up by A. Gianetto and V. Specchia in figure 2.11 [Gianetto and Specchia, 1992].

The standard distribution of the flow profile is very similar to the single phase behavior. The liquid has the tendency to flow at the border of the packing. This is due to a lower resistance to the flow caused by the higher void fractions. This wall effect can be minimized by the shape and the exact areal layout of the filling material. With increasing filling height of the packing in the column the flow at the border from the packing and the column wall rises as well. This effect lead to the installation of intermediate distributors.

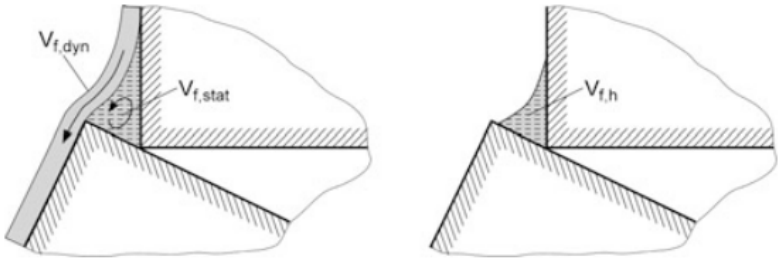

Figure 2.12.: Dynamic and static part of the fluid [Kraume, 2012]

The overall liquid content of the column contains the dynamic and the static fraction of the liquid volume.

$$V_f = V_{\text{f,dyn}} + V_{\text{f,stat}} \tag{2.36}$$

It is a necessary parameter for pre-calculating the important parameters, like the pressure loss or the dimensions of the column. With increasing fluid loading the exchange between the dynamic and the static phase improves. Over a critical load, which is dependent on the packing material (shape and material) and the fluid properties, the static part of the volume disappears.

In figure 2.12 on the left side the volume fraction of the dynamic part and the static part are shown. The dynamic part of the volume fraction $V_{\text{f,dyn}}$ flows over the static part of the volume fraction $V_{\text{f,stat}}$ and lead to a remaining part of the fluid. If the liquid flow stops, at the end of the process or by opening other rivulets the water accumulation and the dissolved material stay back in the gaps.

The static part of the liquid is dependent on the ratio of the force of gravity and the surface tension σ. To describe this in a mathematical way the dimensionless numbers of Weber and Froude are used.

$$We = \frac{\rho v^2 L}{\sigma} \tag{2.37}$$

$$Fr = \frac{v^2}{gL} \tag{2.38}$$

The Froude number describes the ratio between the inertia force and the force of gravity. This value describes the flow in open areas. The Weber number shows the ratio between the fluids inertia compared to its surface tension. This number is used to analyze thin film flows and provides information on droplets and bubbles.

$$\frac{We}{Fr} = \frac{\rho_f \cdot g}{\sigma} \cdot \left[\frac{\varepsilon \cdot d_p}{1-\varepsilon}\right]^2 \tag{2.39}$$

The ratio of the Weber and Froude number, for the liquid phase, deliver an approximation for the behavior of the static volume fraction in the packed bed. The resulting hold up decreases for $\frac{We}{Fr} > 10$ and stays constant for $\frac{We}{Fr} < 10$ [Kraume, 2012].

The velocity distribution is different in each region of the bed. The reason is the unequal distribution of the voids fraction. The gaps near the walls of the column are very big and a huge amount of the fluid trickles through the gaps at the boundary. This wall effect is also called bypass of the packed bed. This effect can be seen in figure 2.13. The bypass must have a higher water velocity then the rest of the packing. This leads to a higher volume flow in the area on the boundary of the packing.

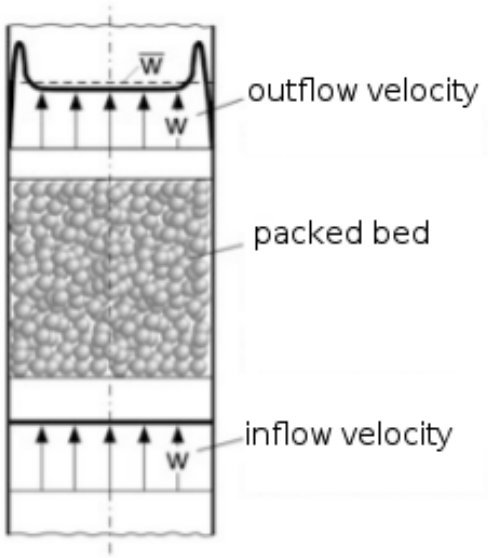

Figure 2.13.: Velocity profile of a packed bed with a single phase flow [Kraume, 2012]

2.3.3. Gas Velocity Distribution

Assuming a constant distribution of our packing, the porosity at each point of the trickle bed has to be the same. In this case we are able to set an average speed for the gas flow through the trickle bed. The free cross section, reduced by the packing, and the mass balance lead to equation 2.40.

$$u_P = \frac{u_0}{\varepsilon} \tag{2.40}$$

In this case u_0 is the superficial velocity that describes the speed of the gas in an empty transverse section and ε is the porosity of the packed bed. In a perfect condition a plug flow or at least a parabolic velocity distribution through the packed bed is expected. In reality the flow speed of the gas depends on the porosity distribution in the packed bed, which leads to a inhomogeneous velocity profile over the packing. Although we have a void fraction of one next to the wall the no slip condition leads to a velocity of zero. By increasing the distance to the wall the velocity strongly increases. The reason for this is the high porosity of the packing in this area. This wall effect which was already mentioned in chapter 2.3.2 is also valid for the gas phase. In the center there is a almost constant porosity [Zeiser, 2008]. This velocity profile can be seen in figure 2.13.

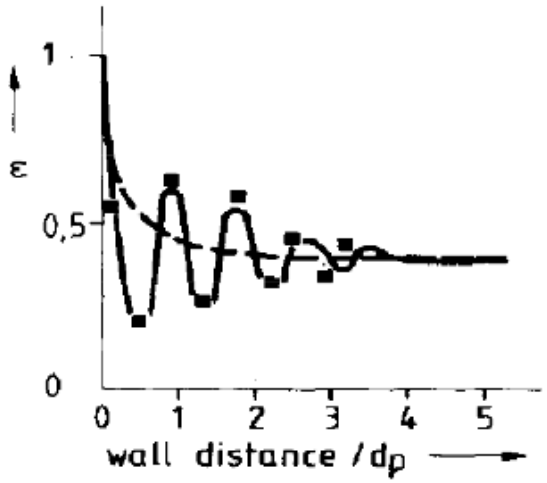

Figure 2.14.: Porosity distribution for spherical particles near the wall [Vortmeyer and Schuster, 1983]

In figure 2.14 the x-axis defines the dimensionless wall distance and the y-axis the porosity of the packed bed. The measured points, which are shown as black squares and the average

porosity can be seen in this diagram. The average porosity was calculated for a circular, in equation 2.41, and a rectangular, in equation 2.42, duct.

$$\varepsilon = \varepsilon_0[1 + Cexp(1 - 2\frac{R-r}{d_p})][VortmeyerandSchuster, 1983] \tag{2.41}$$

$$\varepsilon = \varepsilon_0[1 + Cexp(1 - 2\frac{x}{d_p})][VortmeyerandSchuster, 1983] \tag{2.42}$$

The porosity ε_0 describes the porosity without any wall effects in an infinity packing. The geometrical properties, as the particle diameter d_p and the radius R or the edge length x of the column, are used parameters in these two equations.

Modern measurement technology like the Laser-Doppler-Anemometrie is capable to measure the local velocity distribution in the packed bed in all three dimensions. The evaluation of the conditions in the packed bed are relevant parameters for investigating the transport processes.

2.3.4. Mass-Transfer in Trickle-Bed Reactors

In addition to the macroscopic view of the absorption column, where the flow of the fluids is observed, the microscopic view gives more detailed informations on the mass transfer.

The mass transfer increases with a raising gas flow rate and decreases with an increasing water flow rate, if the gas flow rate remains steady. This phenomena can be described by the different hold up conditions in the absorption column. Also a displacement of the gas phase by the liquid phase takes place. James Ogrill conducted experiments with different flow rates and particles sizes and discovered this behavior in all of his experimental runs [Orgill et al., 2013].

Correlations

A correlation shows the relation between different cases. In case of a trickle bed there are many factors which interact with each other. As well as the volumetric flow and the consequential flow regime, the mass transfer between the gas and liquid phase also has to be

considered. For easy adjustments on the parameter and comparable results dimensionless numbers are a common way to describe the behavior of processes. The most relevant dimensionless numbers are:

- Reynolds number Re
- Weber number We
- Schmidt number Sc
- Sherwood number Sh
- Froude number Fr
- Lockhart Martenelli number X

Also the Eotvos number Eo, the Morton number Mo and the Stanton number St can be used to describe the hydrodynamics in such a process but are not discussed in detail.

Especially for the scale up from laboratory sized to regular units these dimensionless numbers are commonly used in practice. In the following equations the index G stands for the gas and the index L for the liquid phase.

The Reynolds number describes the ratio between the inertial forces and the viscous forces. In case of a trickle bed the liquid phase as well as the gas phase must be mentioned separately. Therefore two different Reynolds number are calculated.

$$Re_L = \frac{v_{\mathrm{sL}} \rho_L d_P}{\mu_L} \tag{2.43}$$

$$Re_G = \frac{v_{\mathrm{sG}} \rho_G d_P}{\mu_G} \tag{2.44}$$

In these equations v_{s} describes the superficial velocity of the respective phase. The characteristic length is the particle diameter. The substance parameters, density ρ and the viscosity μ, are used in the Reynolds number as well.

The Weber number is for two phase flows and provides the ratio between inertia force and the surface forces. The Weber number is also characteristic for both phases.

$$We_L = \frac{{v_{\mathrm{sL}}}^2 d_P \rho_L}{\sigma_L} \tag{2.45}$$

$$We_G = \frac{{v_{sG}}^2 d_P \rho_G}{\sigma_L} \tag{2.46}$$

The Schmidt number provides the relation between the diffusive momentum transfer and the diffusive mass transfer. Both phases have to be taken into account.

$$Sc_L = \frac{\mu_L}{D_L \rho_L} \tag{2.47}$$

$$Sc_G = \frac{\mu_G}{D_G \rho_G} \tag{2.48}$$

The Lockhart Martinelli number is only used for the gas phase but is commonly used for internal two phase flows. With this number the liquid fraction of a flowing fluid can be described.

$$X_G = \frac{v_{sG}}{v_{sL}} \cdot \sqrt{\frac{\rho_G}{\rho_L}} \tag{2.49}$$

Many of these dimensionless numbers have been investigated in different scenarios, in particular the ones that correlate with the hydrodynamics in packed beds. But the gas - liquid mass transfer needs an improvement for these correlations. For the mass transfer the interfacial area is an important parameter. As a consequence the volumetric mass transfer coefficients $k_L a$ on the liquid - or $k_G a$ on the gas side are used for such correlations.

The $k_L a$ and $k_G a$ are based on the Two Film Theory, seen in section 2.2.1, and describe the transport between the boundary. An example is the change of the concentration over time of the transferred component which is dependent on the concentration difference, the area of the mass transfer and the volumetric mass transfer coefficient. The C^* in equation 2.50 describes the equilibrium concentration of the component.

$$\frac{dC}{dt} = k_L a \cdot (C^* - C) \tag{2.50}$$

The mentioned volumetric mass transfer coefficient can be delivered by the Sherwood number for the respective phase. The Sherwood number describes the ratio of the effective mass transfer to a pure diffusion driven mass transfer.

$$Sh = \frac{\beta \cdot L}{D} \tag{2.51}$$

The β in equation 2.51 describes the mass transfer coefficient.

$$\beta = k_i a L \tag{2.52}$$

In 1992 G. Wild invented correlations between the dimensionless numbers mentioned before. In this work the mass transfer is differentiated into the kind of interaction between the faces. The flow regime is separated into low interaction (trickle flow regime), high interaction (pulse flow regime) and the transition. It further distinguishes between the gas and the liquid phase.

In equations 2.54-2.58 d_h describes the Krischer and Kast hydraulic diameter.

$$d_h = d_P \sqrt[3]{16\varepsilon^3/9\pi(1-\varepsilon)^2} \tag{2.53}$$

For low interaction following correlations are mentioned in [Iliuta et al., 1999]

$$Sh_L = 2.8 \cdot 10^{-4}[{X_G}^{0.5} {Re_L}^{0.8} {We_L}^{0.2} {Sc_L}^{0.5} (\frac{a_s d_h}{1-\varepsilon})^{0.25}]^{3.4} \tag{2.54}$$

$$Sh_G = 0.067[{X_G}^{0.5} {Re_L}^{0.8} {We_G}^{0.2} {Sc_G}^{0.5} (\frac{a_s d_h}{1-\varepsilon})^{0.25}]^{1.1} \tag{2.55}$$

As well as the correlations for high interaction:

$$Sh_L = 0.45[{X_G}^{0.5} {Re_L}^{0.8} {We_L}^{0.2} {Sc_L}^{0.5} (\frac{a_s d_h}{1-\varepsilon})^{0.25}]^{1.3} \tag{2.56}$$

$$Sh_G = 0.123[{X_G}^{0.5} {Re_L}^{0.8} {We_G}^{0.3} {Sc_G}^{0.5} (\frac{a_s d_h}{1-\varepsilon})^{0.25}]^{0.9} \tag{2.57}$$

In equation 2.57 the transition between those two regimes are also considered. For the liquid phase a special correlation for the transition is shown:

$$Sh_L = 0.091[{X_G}^{0.25} {Re_L}^{0.2} {We_L}^{0.2} {Sc_L}^{0.3} (\frac{a_s d_h}{1-\varepsilon})^{0.25}]^{3.8} \tag{2.58}$$

In 1985 Yaici W. described another correlation for the gas side that can be used for all regimes [Yaici W., 1985].

$$Sh_G = 0.049(a_x d_P)^{-0.015} Re_G^{1.08} Re_L^{0.2} Sc_G^{0.5} (\frac{d_P}{d_c})^{0.72} \tag{2.59}$$

The ratio between the liquid interfacial area a to the external area of particles and wall per unit reactor volume a_s is an important parameter for trickle bed reactors.

$$a_s = 6\frac{(1-\varepsilon)}{\phi} d_P + \frac{4}{d_c} \tag{2.60}$$

In equation 2.60 d_p stands for the particle- and d_c for the column diameter. ϕ displays the sphericity factor. Again this formula distinguishes between the different flow regimes.

The equations 2.61, 2.62, 2.63 show the correlations for the low, high and transitional interaction.

$$\frac{a}{a_s} = 10[X_G Re_L^{-0.5} We_L (\frac{a_s d_h}{1-\varepsilon})^{1.5}]^{0.7} \tag{2.61}$$

$$\frac{a}{a_s} = 21.3[X_G Re_L^{-0.5} We_L (\frac{a_s d_h}{1-\varepsilon})^{-2.0}]^{0.5} \tag{2.62}$$

$$\frac{a}{a_s} = 1550[X_G Re_L^{-0.5} We_L (\frac{a_s d_h}{1-\varepsilon})^{-5.0}]^{0.7} \tag{2.63}$$

Potnis and Lenz showed another correlation for random packed trickle beds and the mass transfer. A ratio between the wetted surface, a_w, and the total surface, a_t, is described. In contrast to 2.61, 2.62, 2.63 the surface tension of the liquid phase σ and the critical surface tension σ_c are also used in this equation [Potnis and Lenz, 1996]. The critical surface tension describes the required tension to completely moisten a solid body.

$$\frac{a_w}{a_t} = 1 - exp[-1.45(\frac{\sigma_c}{\sigma})^{0.75} Re_G^{0.1} Fr^{-0.05} We^{0.2}] \tag{2.64}$$

This equation is valid between the following limits.

$$0.04 < Re_L < 500 \tag{2.65}$$

$$1.2 \cdot 10^{-7} < We < 0.27 \tag{2.66}$$

$$2.5 \cdot 10^{-9} < Fr < 1.8 \cdot 10^{-2} \tag{2.67}$$

$$0.3 < \frac{\sigma_c}{\sigma} < 2 \tag{2.68}$$

The transfer of the molecules between the phase surfaces occurs from the turbulent area through the laminar boundary layers of both media. The resistance to the mass transfer is connected directly to the thickness of these layers. The thickness of these layers can be calculated by many different parameters such as transport properties or the velocity of this layers. Bird, R.B. [Bird, 2007] shows the thickness of such a layer in the following equation.

$$\delta = C_1 \sqrt{\frac{\mu}{\rho} \frac{X}{v_\infty}} \left(\frac{D\rho}{\rho}\right)^{1/3} \tag{2.69}$$

In equation 2.69 C_1 shows a constant, that is dependent of the velocity profile in the boundary layer. Therefore the Reynolds number and the Schmidt number are the most important parameters.

$$Sh = CRe^{a}Sc^{b} \tag{2.70}$$

In this work the Schmidt number was kept constant and the dependence of the flow rate on mass transfer was analyzed. The Two Film Theory, see section 2.2.1, is based on the idea, that the mass transfer coefficients are directly proportional to the diffusivity and that the film between those phases is stagnant. In a moving system the Film Theory cannot be considered. In this case the Penetration Theory and the Surface Renewal Theory are more accurate approaches.

Depending on the geometrical properties and the boundary conditions of the absorption column different solutions for the constants appear. In the work of Potnis and Lenz, [Potnis and Lenz, 1996], a combination of a dehumidifier and a regenerator has been investigated. For this special case the following correlation have been investigated.

$$Sh = 0.46 Re^{1.2} Sc^{0.5} \tag{2.71}$$

$$Sh = 0.8 ReSc^{0.5} \tag{2.72}$$

Equation 2.71 shows the correlation for the regenerator and equation 2.72 shows the correlation for the dehumidifier. With this approach a nongeneral valid correlation has been invented, but it can be used to calculate approximations for a special cases and related approaches.

Another way to describe the mass transfer has been explored by Onda K. [ONDA et al., 1968]. This concept is not based on dimensionless numbers.

$$k_l (\frac{\rho_l}{\mu g})^{1/3} = 0.0051 (\frac{L*}{a_w \mu})^{2/3} (\frac{\mu}{\rho_l D})^{-1/2} (a_t D_p)^{0.4} \tag{2.73}$$

2.3.5. Holdup and axial dispersion

The liquid holdup defines the volume fraction of the liquid, referred to the total bed volume that remains in the bed after the bed is completely drained [Saez et al., 1991].

The holdup consists of two parts, on the one hand the internal and on the other hand the external holdup. The external hold up contains the water that is stored due to geometrical reasons of the particles. The internal hold up is caused by the material of the particle. A porous packing has a big capacity for storing the liquid phase. This greatly influences on the resistance time and furthermore on the mass- and heat transfer [Fu and Tan, 1996].

The ideal flow and the actual flow in technical devices differ from each other. A ideal plug flow is rare and the related behavior can be seen in figure 2.15. The residence time of a phase in a column is a proper way to describe the behavior of the media while trickling down the packing. The dispersion coefficient D_{ax} (m^2/s) represents this process [Levenspiel, 1999].

- large D_{ax} means rapid spreading of the tracer curve
- small D_{ax} means slow spreading
- $D_{ax} = 0$ means no spreading, hence ideal plug flow

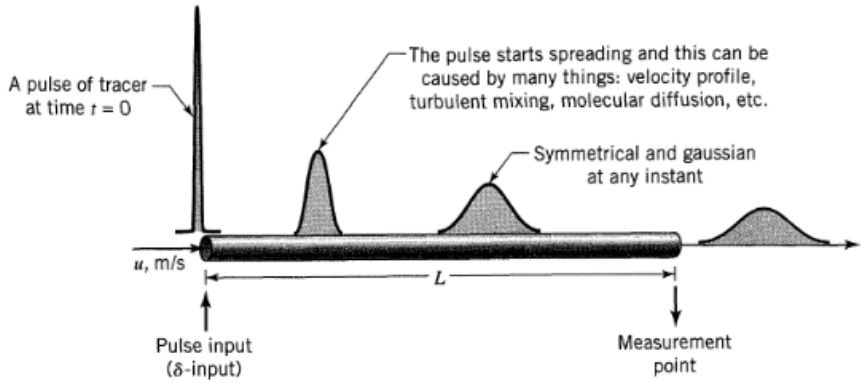

Figure 2.15.: Spreading of a the tracer in a pipe [Levenspiel, 1999]

To evaluate the dispersion coefficient the shape of the output tracer curve of the reactor can be used. Important parameters are the mean time of the dilution $\bar{t}$ and the variance σ^2, which can be measured by the spread of the curve. In figure 2.16 the difference between two experiments is shown. A pulse of a tracer was added on the input and the concentration of the inserted substance is measured at the output. While in A an increasing dispersion and backmixing occurs, B shows a more likely plug flow behavior. Instead of the dispersion coefficient, the dimensionless relation can be used as well $\frac{D_{ax}}{uL}$.

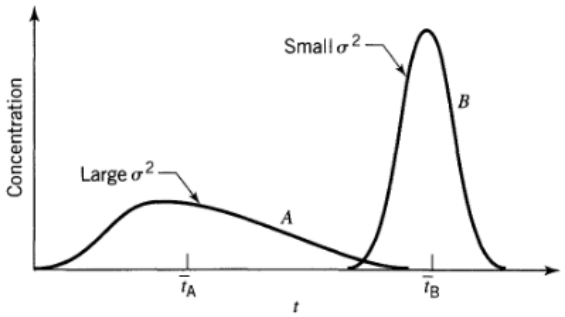

Figure 2.16.: Different residence time and variance [Levenspiel, 1999]

The dispersion coefficient can be introduced by the second law of Fick.

$$\frac{\partial C}{\partial t} = D\frac{\partial^2 C}{\partial x^2} \tag{2.74}$$

The difference between diffusion and dispersion is the mechanism. Diffusion describes the spreading of material due to the random motion of the molecules. The dispersion consider a convective flow superposed over the diffusion.

In equation 2.74 D describes the diffusion coefficient. The intermixing of the fluid flow can be characterized in a similar way. The equation to describe the behavior of the fluid flow is equal to equation 2.74. D_{ax} is, as mentioned before, the axial dispersion coefficient and characterizes the backmixing during a process. This equation shows the mixing only in one direction. In case of an axial consideration this is sufficient. For a dimensionless approach some modification have to be made [Levenspiel, 1999].

$$z = \frac{ut + x}{L} \tag{2.75}$$

$$\theta = \frac{t}{\bar{t}} = \frac{tu}{L} \tag{2.76}$$

With the adjustments, equation 2.75 and 2.76, the balance for the concentration of a species can be calculated as seen in figure 2.17.

$$\frac{\delta C}{\delta \theta} = (\frac{D_{\text{ax}}}{uL})\frac{\delta^2 C}{\delta z^2} - \frac{\delta C}{\delta z} \tag{2.77}$$

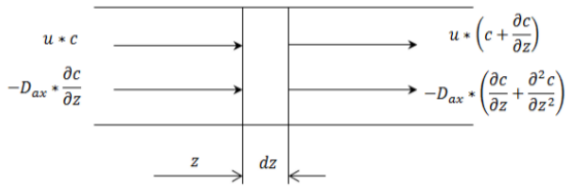

Figure 2.17.: Species balance for a volume element with axial dispersion [Prieler, 2012]

In the dimensionless balance in equation 2.77 the reciprocal of the Bodenstein number is used.

$$Bo = \frac{u \cdot L}{D_{\text{ax}}} \tag{2.78}$$

This dimensionless number provides the ratio between the convective and the diffusion of the introduced species. It describes the axial distribution of the fluid in the column. An increasing

Bodenstein number is more similar to a standard plug flow. Consequential a decreasing Bodenstein number shows a improved distribution in the packed bed.

The backmixing decreases the concentration difference over the column height. In case of a countercurrent gas - liquid absorption process without backmixing a mass transfer gradient will occur over the packed bed. At the bottom of the column the liquid is already loaded with the absorbed species. At the top of the packing the liquid starts with the absorption. At higher flow rates, when backmixing takes place the mass transfer gradient becomes more blurred over the height of the column and the residence time in the absorber increases. These two events lead to a absorption process with higher yield of the substance.

Determination of the axial dispersion coefficient

Levenspiel showed different behaviours of reactors depending on the the axial dispersion coefficient, the average velocity of the liquid and the length of the packing.

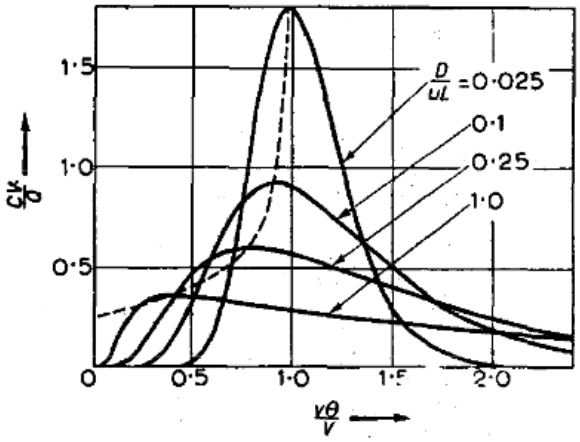

Figure 2.18.: Curves for different residence time behavior [Levenspiel and Smith, 1957]

In figure 2.18 the x-axis shows the dimensionless time and the y-axis the ratio between the amount of substance and the volume of the tracer which will respond to the actual amount of the tracer. This can also be described by the dimensionless output to a pulse input or the exit age distribution. In the following this output value will be called E, as described by Levenspiel and Smith [Levenspiel and Smith, 1957].

$$E_t = \frac{u}{\sqrt{4\pi D_{ax} t}} exp(-\frac{(L-ut)^2}{4D_{ax}t}) \tag{2.79}$$

For a dimensionless residence time curve the time gets normalized with

$$\theta = \frac{t}{\tau} \tag{2.80}$$

$$E_\theta = \frac{1}{\sqrt{4\pi \frac{D_{ax}}{uL}}} exp(-\frac{(1-\theta)^2}{4\theta \frac{D_{ax}}{uL}}) \tag{2.81}$$

Correlations of the axial Dispersion Coefficient

Due to the importance of the axial dispersion many studies have already dealt with this issue. The most important dimensionless number in this case is the Peclet number which has the same definition as Bodenstein number, but instead of the dispersion coefficient the diffusion coefficient is used. The Peclet number is equal to the Bodenstein number in equation 2.78. The state of knowledge for the dispersion coefficient is that the diffusion and the convection are coupled in this parameter [Ligny, 1970].

Seyed R. and Tingyue G. [Seyed and Tingyue, 2017] collected data to evaluate a correlation for the Peclet number in fixed bed columns. This correlation was fitted to experimental data and shows a relation between the Peclet- and the Reynolds number.

$$\varepsilon Pe_p = 0.18 + 0.008 Re^{0.59} \tag{2.82}$$

This equations includes the porosity ε and the Peclet number, which refers to the particle diameter. The Reynolds number is explained with the equation 2.83.

$$Re = \frac{d_p v_s \varepsilon \rho}{\mu} \tag{2.83}$$

This equation uses the superficial velocity v_s. The problem of using this correlation and all equations that are based on it, is that they only investigate the liquid flow through a trickle bed without the countercurrent air flow. The countercurrent upflow of the gas phase gives the liquid phase less place to flow through the packing. In this case a higher velocity occurs and the superficial velocity cannot be used. As the gas phase is not included in this calculations the Peclet number stays constant for all air flow rates.

In a two phase system the evaluation is more complicated. In the literature different approaches can be found. The results differ from each other and a general validity can not be found [Ram, 1966]. This is due to the fact that there are countless possibilities to run an absorption column. The changes of the parameters can be geometrical, of the flow conditions or of the packing. In 1962 Otake et. al. invented a correlation for a countercurrent flow in a trickle bed filled with Raschig rings [Otake et al., 1962]. In this equation the Galilei number is used. This number shows the ratio between the gravitation force and inner friction forces.

$$Ga = \frac{gL^3}{\vartheta} \tag{2.84}$$

In this equation L stands for a characteristic length, g for the force of gravity and ϑ for the kinematic viscosity. The correlation from Otake, [Otake et al., 1962], shows the Peclet number dependent to the Galilei and the Reynolds number for the liquid phase.

$$Pe = 1.425(Ga)^{-0.333} {Re_L}^{0.777} \tag{2.85}$$

In 1958 another correlation was invented by Aris Rutherford [Ram, 1966]. This correlation was introduced with two phase flow conditions.

$$Pe_L = 19.4(\frac{dL}{\mu})^{0.747}(\frac{d^3 g \rho^2}{\mu^2})^{-0.69}(ad)^{1.97} \tag{2.86}$$

a in this equation stands for the surface area of packing per unit volume of the packed bed. The velocity of the liquid mass flow, L, was also used in this investigation. Another approach to calculate the Peclet number was invented by Demaria and White in 1960 [Demaria and R. White, 1960]. In this correlation both phases, liquid and gas, are used to predict the dispersion of the liquid phase in the packed bed.

$$Pe = 2.4(Re_G)^{0.2} \cdot 10^{-(0.013 - 0.088\, d_p/d_t)Re_L} \tag{2.87}$$

This equation includes the Reynolds numbers for both phases to define the flow conditions. The trend of this correlation is the same as for the experimental evaluated data.

Chapter 3.

Experimental Setup

The base of the experimental setup is the bubble column, which was built by Michael Lukasser in 2008. The challenge was the revitalization of the old device and to set it up in its new location. For that reason it was dismounted completely and the core, which consists of the aluminum frame and the glass cuboid in the middle, was transported to the new destination. All other parts where checked and if necessary repaired or adapted. The operation mode, bubble- / absorption column, could be changed without extensive modifications.

For detailed information of the bubble column see the master thesis of Michael Lukasser [Lukasser, 2008].

3.1. Aluminum Frame and Collection Tray

The old and bigger collection tray was recycled to create the new one, which is smaller so the device can fit in its new spot. The size of the new one was assessed by the maximum liquid content of the glass part, which has a height of two meters and an edge length of 0.2 meters. The maximum liquid content of the glass cuboid is 80 liter. The size of the new collection tray resulted in the dimensions 110x110x10 (LxDxH)cm. Due to the smaller area the construction of the braces on the ground was also changed to a smaller dimension. The decreased stability, which occurred because of the smaller area on the bottom of the construction, was compensated with an aluminum profile on the top which was mounted to the wall. The aluminum profile construction in the back of the column for the pumps, lower level, and the control box, upper level, was added. The storage tank is located at the bottom of the aluminum construction to create a higher stability with its weight.

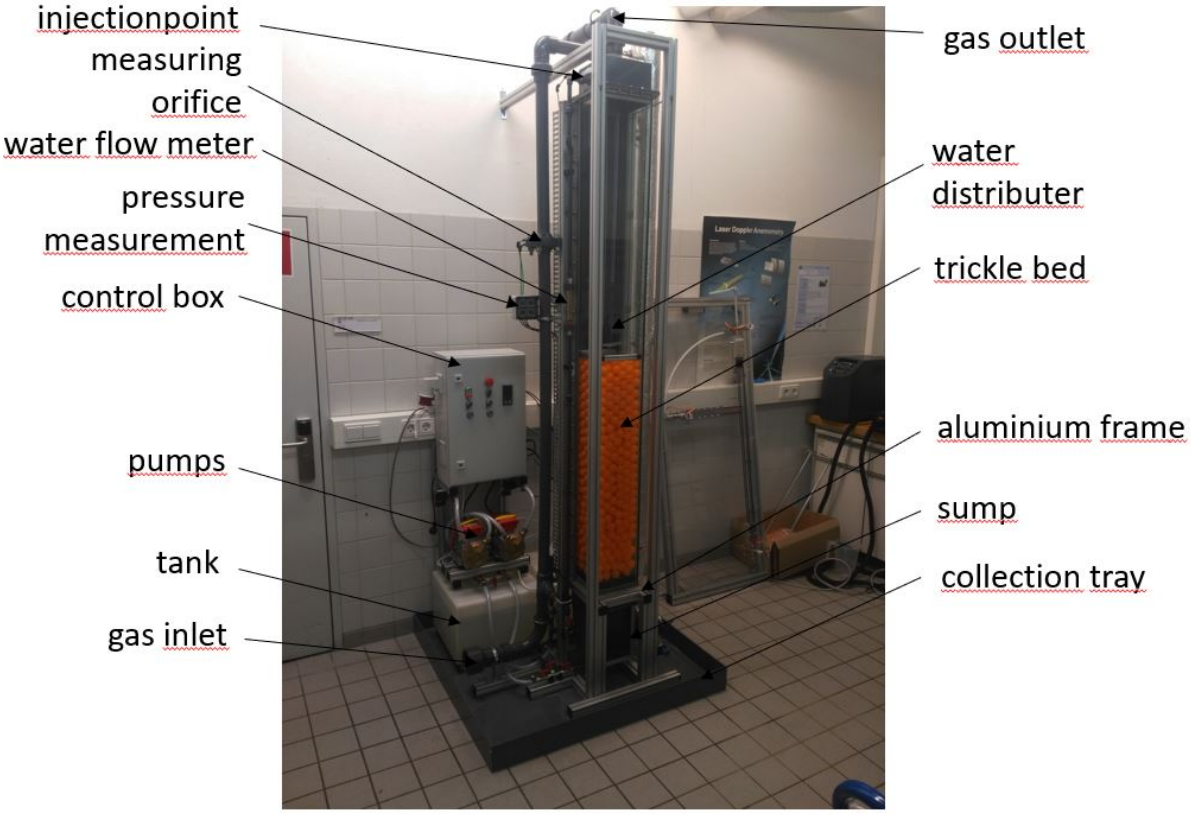

Figure 3.1.: Experimental Setup

The glass cuboid was left in the steel frame and has not been altered. The backplate of the column was exchanged with a nontransparent PVC plate, which also had been adapted for the oxygen concentration and conductivity measurement.

To prevent the packing from floating a steel mesh was added on the top of the packing. This mesh was attached to a built frame, with the dimensions of the inner glass cuboid. This frame was fixed with four threaded rods, one for each corner, to the top of the column. The mesh can be seen in figure 3.5(b).

3.2. Piping and Measurement

A few points in the existing PVC piping were modified, but the functionality of the old system has not changed much.

For documentation and a better overview of the experimental setup a piping and instrumentation diagram (P& ID) was created. For this task Autodesk Plant 3D was used. The P& ID can be seen in appendix A.

Due to the geometrical changes the length and the arrangement of some pipes had to be adapted. Some parts broke and got repaired. The sealings were replaced completely. The tubes were remodeled completely.

3.2.1. Piping

The inlet for the gas phase was adapted. It was now possible to insert the air by two different devices, a blower and a compressor. The air inlet could be changed easily by mounting the belonging design via a thread (3.2). Next to the air inlet an additional gas feed was added to mix the ambient air with other substances. To handle the second inlet a valve was mounted (figure 3.2).

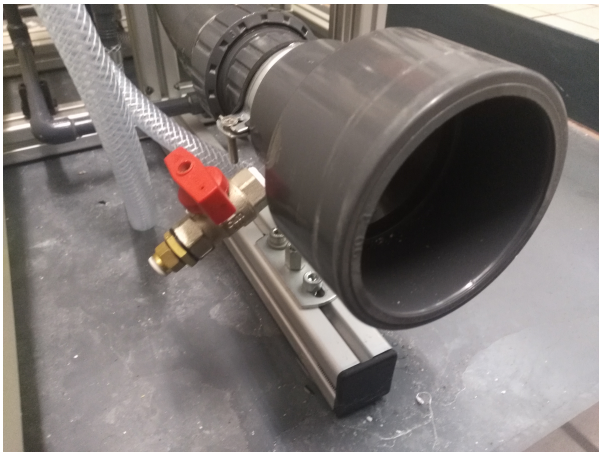

Figure 3.2.: Air- and additional gas inlet

To measure the volume flow rate of the air a new measuring orifice according to DIN EN ISO 5167-2 standard was built. This measurement was based on the pressure before and after the orifice. For this reason the existing holes for the pneumatic tubes were adapted. The old insolation around the heater pipe was changed particular. For safety reasons an overpressure valve was added at the end of the air pipe before it enters the sump of the column (figure 3.3). The existing gassparger was not changed but it was repaired and sealed again.

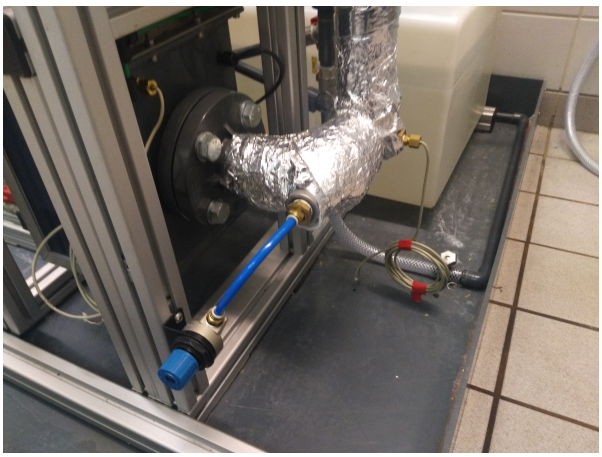

Figure 3.3.: Safety valve and temperature sensor (PT100) after heater

The top plate of the tank was modified and adjusted to the new water distributor. A longer suction pipe was added and a filter, to avoid dirt particles in tWith an extra tube, which had to be mounted on the pressure side of the second pump the water could be delivered direct to the drain to avoid a contamination of the water in the tank. The working direction of the pumps can be changed. For that reason manual valves between the pumps were added to control the direction of the flow. With the valve cross on the back of the column it is possible to let the water flow in different directions and run the column in different modes. For the water distribution on the top of the experimental setup a tube was added from the bottom of the cross to the riser. To measure the water flow to the water distribution unit a flow meter with a range of zero to 320 l/h was implemented (figure 3.4).

Figure 3.4.: Flowmeter for determining the water flow

To determine the residence time of the water in the column a position for injecting a liquid tracer was added in a pipe, next to the top of the column (figure 4.6(a)). For the injection of the tracer a syringe is used. The syringe leads to a valve, that can be closed when no injection is implemented. The old spray device on the top of the column was removed and replaced by a new one. The old and the new water distribution units can be changed with the existing thread inside the top of the column. The new distributer consists of a PVC pipe, which enters in the middle of the column from the top to five cm over the packing. The last part of the pipe was built out of transparent plastic to observe the pipe flow and detect air bubbles. The tip of the water distribution unit has four holes in a 45°angle to provide a better water distribution on the top of the bed. Before mounting the water flow had been tested in the laboratory. The tip leads the water to the trickle bed without splashing directly onto the column wall. The water distribution was in the whole range of 50 l/h to 320 l/h acceptable. The experimental setup of the tests can be seen in figure 3.5(a). The grey fixing unit guarantees the position of the distributor. The water distribution on top of the trickle bed is shown in figure 3.5(a).

The existing pipe for draining the sump was replaced. To empty the column without pumps

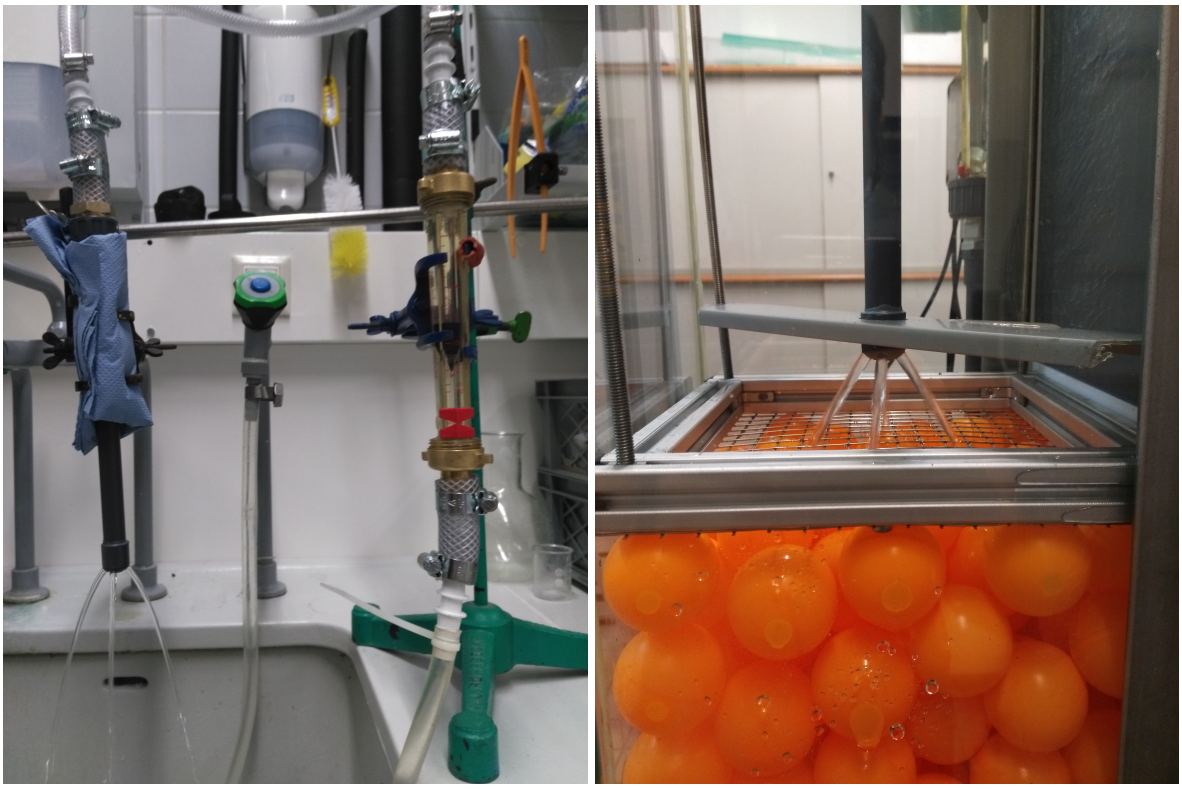

(a) Water distributor tested in laboratory (b) Water distributor during an experiment

Figure 3.5.: Water distribution unit

an additional T-piece was added. Each direction of the T-piece can be opened and closed by valves. Because of that it is possible to empty the column as long as the hydrostatic pressure is sufficient. Due to the height differences of the column and the tank the remaining water will just stay in the sump. In the sump a LED light, which has no contact to water in the sump, was added. The reason for including this light was to get a better view in the sump when the column is turned on to observe the water level in the sump.

3.2.2. Pressure and Temperature Measurement

The existing measurement probes were removed and replaced completely. New pressure sensors were added at four points of the setup. Two are added at the flange on the raiser, one is mounted at the bottom and one at the top of the column. The two measuring points in the sump and on the top of the column measure the pressure loss over the perforated plate and the packing. For these measurement points new holes were drilled and clutches for the

pneumatic tubes added. The pneumatic tubes lead to the pressure measurement devices. The way of tubes to the devices were chosen as short as possible with avoiding wrinkles.

Figure 3.6.: Local pressure measurement of all four measuring points

Those pressure devices are powered from 24V supply directly in the control box. The sump and the top of the column were also extended with new a PT100 temperature sensor. For this new measurement devices holes had to be redone and sealed. Another PT100 temperature sensor was mounted at the outlet of the heater. A humidity sensor was implemented in the raiser of the air pipe. The cabling of these sensors was hidden as well as possible, mostly in the frame of the column. For the rest of the cables an extra cable channel was added to the back of the column. For the experiments the data processing was done in an analog way. For measuring of the oxygen levels in the air, the pneumatic tube leasing to the safety valve was removed and replaced by a 90°elbowpipe bow, in which the sensor fits. Fortunately an extra exit on the gas outlet already existed where the other sensor was mounted with a 90°elbowpipe.

3.3. Control Box

The control box, figure 3.7, was built up from scratch. The duties of this unit are on the one hand to provide the electrical energy and on the other to control the separate units. In the future another unit will be added for data equisition and processing.

Figure 3.7.: Control Box

The control box is plugged into a single phase 230 V and a three phase socket 400 V power socket. The 230 V circuit supplies a transformator, the 24 V power supply the Siemens LOGO! control unit, the control unit of the heater and the relays. The three phases of the 400 V circuit are split to provide the power for the two frequency converters for the pumps and the heater. The frequency converters and the heater are controlled over separate relays. A power meter measures the power consumption of the heater. The units can be separately switched outside of the control box. A fan provides an airflow threw the control box.

A detailed drawing of the circuit diagram was created with sPlan 7.0. The circuit diagram and a list of all units can be seen in appendix A.

3.3.1. 230 V Circuit

As mentioned before, the control box utilizes two different conductor rails. After entering the 230 V rail a 30 mA residual current circuit breaker secures this area. As seen on the circuit diagram the fan is powered directly to this rail and is secured with a melting fuse. The transformer and the 24 V power supply are connected directly but are secured with an extra fuse. To provide the energy for holding the relay the 230 V circuit is used as well. The relays can be turned on or off by a switch on the outside of the control box which also contains an indicator LED. The temperature control of the heater is also supplied by this unit and secured by a melting fuse. The 24 V power supply provides the energy for the Siemens Logo! control unit which operates the magnetic valves when the pump is turned on.

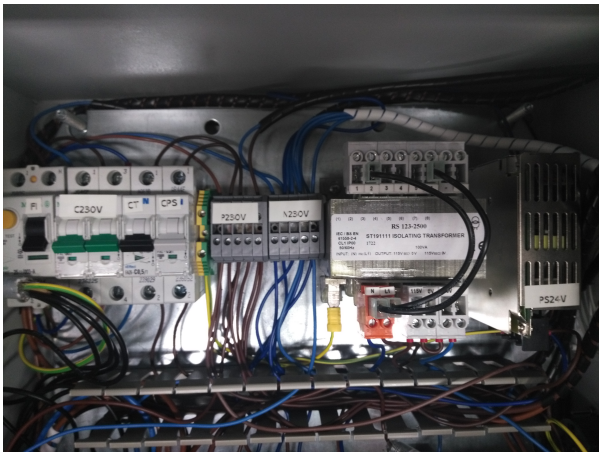

Figure 3.8.: 230V rail of the control box

3.3.2. 400 V circuit

The 400 V circuit contains three 230 V phases which are used seperately. Two of the phases are used for the pumps and one for the heater. Over a protective block the electricity enters the circuit and is secured by a Siemens Sirius closing unit. This unit can be controlled by the on/off switch and the emergency stop button on the outside of the control box. The on/off switch is also visualized with a LED. Each unit is switched by a relay. The first two phases are providing the energy for the two pumps indirectly over two frequency inverters. The frequency inverters can be controlled with a remote control, built by Bahram Haddadi (figure 3.9). With this unit it is possible to set the speed and the running direction of the pumps without opening the control box.

Figure 3.9.: Remote control unit for both pumps

The third phase provides the energy for the gas line pre-heater. An electric power meter detects the required current and gives information about the heating power. This measurement tool is also secured by a melting fuse. A transformer provides a 24 V supply to the heater control unit from the 230 V line.

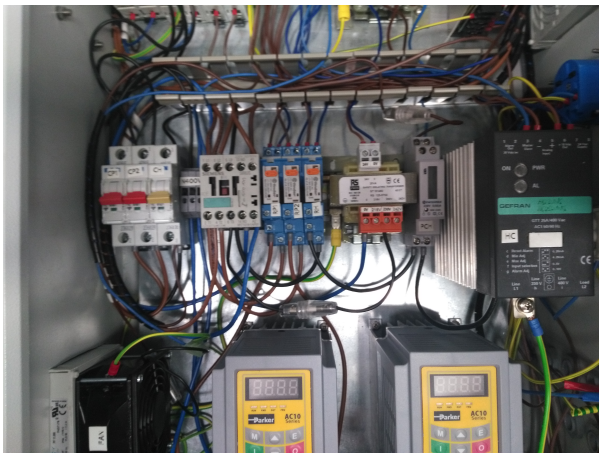

Figure 3.10.: 400 V rail of the control box

3.4. Perforated Plate

Because of the special requirements for the packed bed absorption process and the measuring of the oxygen content of the water a new perforated plate was required. The base size of this perforated plate is the same as the ones which were used by Michael Lukasser [Lukasser, 2008]. The idea of this plate is to provide a water reservoir for the oxygen measurements and holes for the air which will stream up into the column. In the middle of the plate a drain was implemented so the water can change continuously and the old saturated water does not remain in this pit. The weir in the middle of the plate was built with a PVC pipe with 20 mm outside diameter. In figure 3.11 the bottom plate is already mounted to the column. The 20 mm PVC pipe leads from the top of the weir directly to the bottom of the sump. If the sump is filled with water up to 1/3 of its capacity, the air from the sparger flows only directly through the small holes into the bottom plate without streaming threw the 20 mm pipe in the middle.

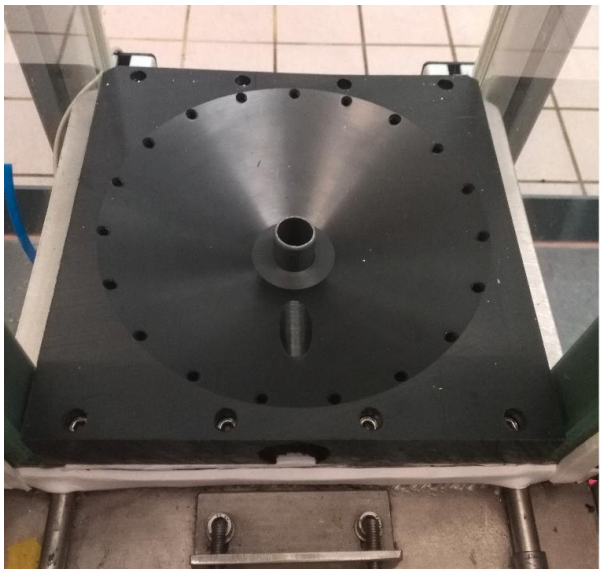

Figure 3.11.: Bottom Plate mounted in the column

To avoid to blockage of the holes with the packing a rough metal mesh was added over the perforated plate. A rough mesh was used to avoid influence on the experiments.

The design drawing of the new bottom plate was created with Autodesk Inventor 2018. This drawing was used for the workshop to construct this part. The detailed construction drawing can be seen in appendix A.

For inserting the probe a hole was drilled at the same position, where the perforated plate has its drilling for the probe. For easy exchanging of the probe a sleeve was added, which seals with two o-rings. To avoid leaking silicon was added on the edges (figure 3.12).

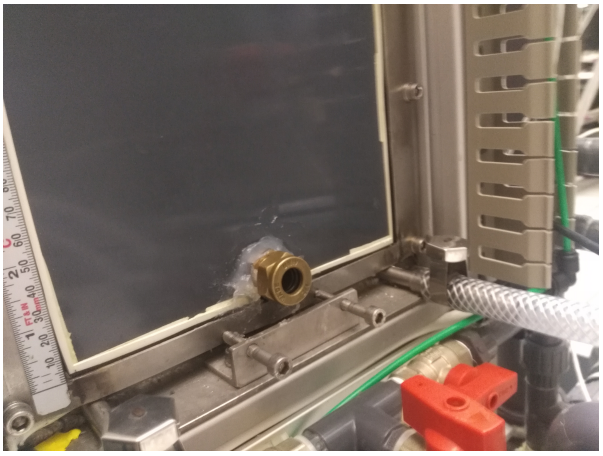

Figure 3.12.: Probe placing on the back of the column

3.5. Measuring Orifice

For the air distribution an existing blower, a side channel blower of the company Becker, was used. The power of the blower is controlled by a frequency innverter which provides an electrical input. Because of the variable pressure loss at the output of the blower and different conditions of the setup, it is not possible to set an air mass flow rate for a specific electrical signal. In this case a measuring orifice is used to measure the actual mass flow. To create and calculate the measuring device the standard DIN EN ISO 5167-2 was followed. The base of this mass flow measuring is the pressure drop between the both sides (1-2) of the orifice 3.13. The measuring points for the pressure are located on the flange. The new measuring orifice has a hole diameter of 16 mm. The diameter D of the orifice is 4.52 cm.

The measuring orifice was build as mentioned in the standard EN ISO 5167-2.

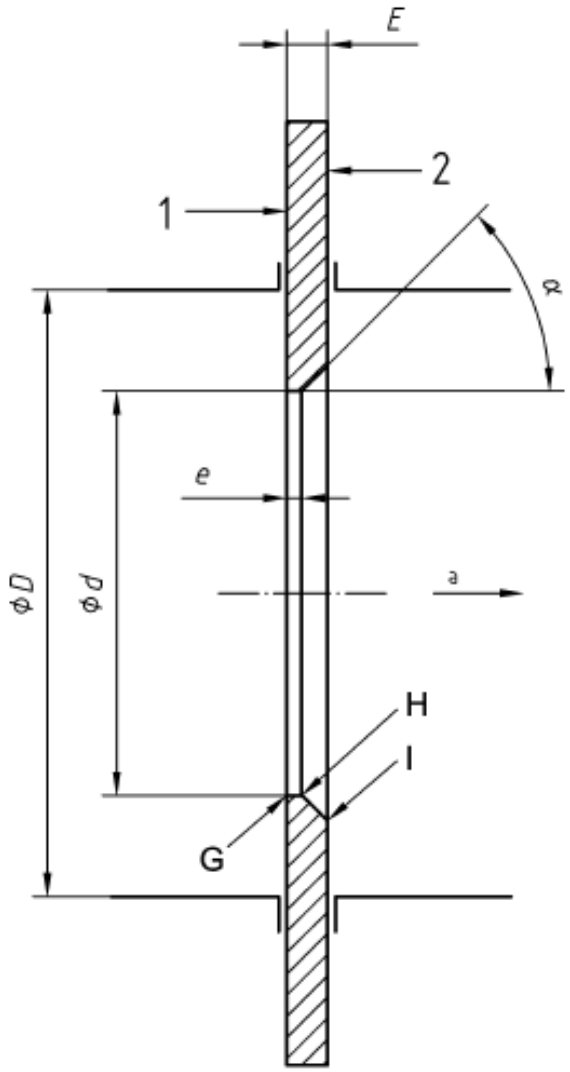

Figure 3.13.: Standard measuring orifice

Chapter 4.

Experimental Data

4.1. Trickle Bed

The filling material for the trickle bed consists of standard table tennis balls. This filling material does not act catalytic but creates a bigger surface for the mass transfer. The bed is filled in a randomly, so the result of the filling behaves like a random packing.

A sample of 75 balls has been chosen to obtain the geometrical properties of the filling material. The average weight w of this sample was 2,102 g and the average diameter was measured to 34,263 mm. With the following volume of a ball the average density of the packing was calculated.

$$\rho_S = \frac{w}{V} = 99,83 \frac{kg}{m^3} \tag{4.1}$$

The absorption column is filled with 774 of these table tennis balls. The height of the packing is 95 cm from the perforated plate mesh to the top edge of the last ball.

4.2. Porosity of the Packing

As already seen in figure 2.14 the porosity is depends on the region. To set a value for this parameter the average porosity over the whole packing was chosen. [Brauer, 1971] shows a formula (4.2) for cylindric trickle bed reactors.

$$\varepsilon = 0.375 + 0.34\frac{d}{D} = 0.44 \tag{4.2}$$

d in this equation stands for the particle diameter and the D for the diameter of the whole column. In the case of a squared column, the hydraulic diameter, which is equal to the edge length, was chosen. To check this value the porosity was calculated out of the void space V_v.

$$\varepsilon = \frac{V_v}{V} = 0.42 \tag{4.3}$$

In both cases the calculated values are close to each other. The reasons for that they are close are imprecisions in measurement and the wall effects to the packing. These results are still in the range of the standard sphere packing which is between 0.4 and 0.45. The porosity was also measured in the virtual packing which was created using a DEM, discrete element method, for the simulation. The porosity in this simulated packing is 0.4. This value was calculated by the function integrate variables in Paraview which provides the volume of the hollow space volume of the packing.

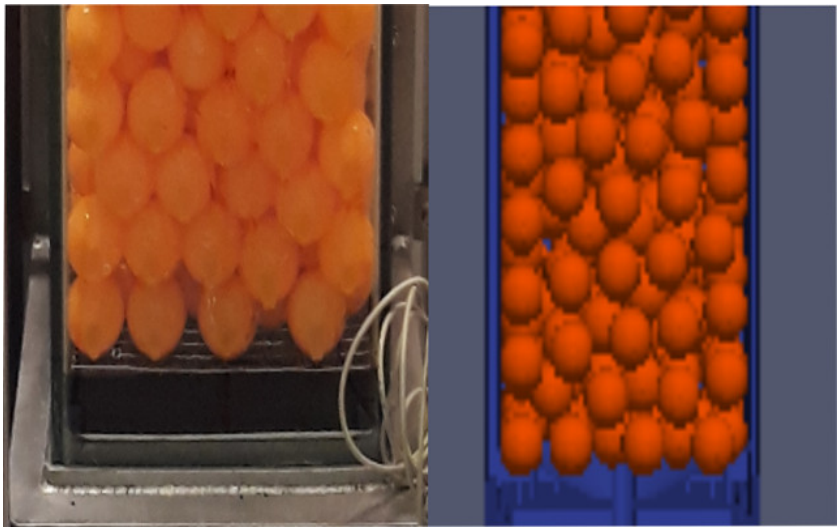

Figure 4.1.: Comparison of the real and the simulated packing

Figure 4.1 shows the similarity of the packing created by the discrete element method simulation and the packed bed of the experimental setup.

4.3. Pressure Loss

The pressure in the absorption column can be measured at the top and in the sump of the column. The pressure loss can be measured between the perforated plate and the packed bed, but must be calculated separate for the perforated plate p_V and the packing p_t.

$$\Delta p = \Delta p_t + \Delta p_V \tag{4.4}$$

4.3.1. Packed Bed

It makes a big difference whether the packing is dry and not sprinkled or moistened. A small water flow rate already increases the pressure loss by about 20 % [VDI, 2013]. The dry pressure loss is calculated as mentioned in the VDI - Waermeatlas [VDI, 2013].

$$\Delta p_t = \zeta \frac{\rho_G u^2_G}{2} \frac{(1-\varepsilon)H}{\varepsilon^3 d_p} \tag{4.5}$$

The resistance coefficient ζ can be taken from figure 4.2.

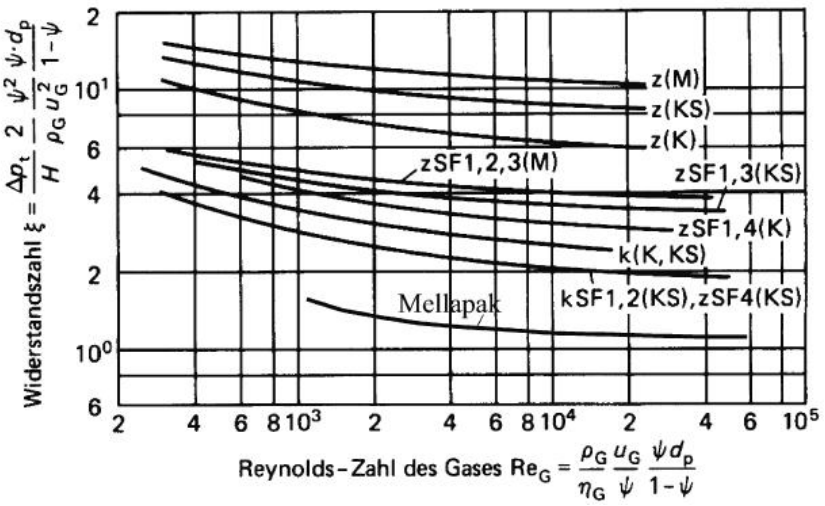

Figure 4.2.: Resistance coefficient over Reynolds number [VDI, 2013]

For a sphere, like the table tennis balls, the function k(K,KS) is chosen. In equation 4.5 it is possible to see, that this equation only depends on the superficial velocity of the gas.

4.3.2. Perforated Plate

The pressure loss of the perforated plate is calculated as mentioned in the VDI - Waermeatlas [VDI, 2013]. In this calculation the ratio between the length s and the diameter of the hole itself d_h makes a big difference. In this case the ratio between these two values is much larger than 0.

$$\frac{s}{d_h} >> 0 \tag{4.6}$$

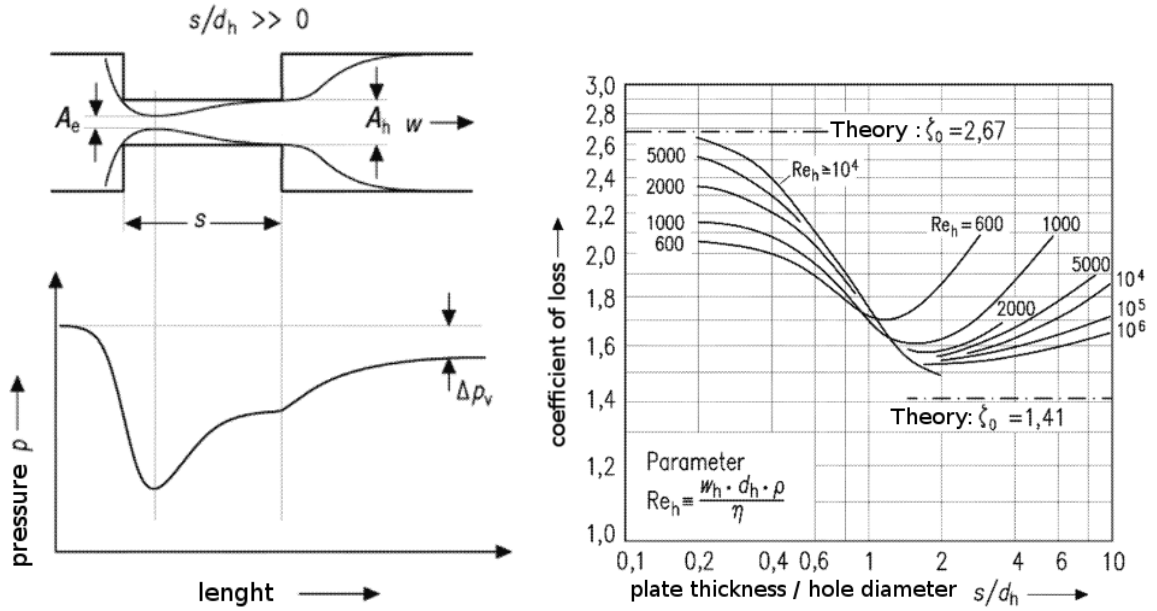

(a) Streaming conditions in a single hole [VDI, 2013]

(b) Correlation of the coefficient of loss for a hole [VDI, 2013]

Figure 4.3.: Flow conditions in a hole and coefficient of loss

The pressure loss Δp_V through the perforated plate is calculated with equation 4.7. The velocity of the fluid flow w before and after the hole, the velocities of the smallest cross section, w_e, and the velocity in the full cross section of the hole w_h are used in this equation. The velocities and their belongings can be seen in 4.3(a).

$$\Delta p_V = \frac{\rho}{2} \cdot w^2{}_h \cdot (\frac{w_e}{w_h} - \frac{w}{w_h})^2 \tag{4.7}$$

In equation 4.7 the resistance coefficient is equal to the term in the brackets squared.

$$\zeta = (\frac{w_e}{w_h} - \frac{w}{w_h})^2 \tag{4.8}$$

The coefficient of loss ζ_0 is converted to ζ. For our case, s/d » 0, the conversion is seen in equation 4.9. The value for ζ_0 is illustrate by figure **??**.

$$\zeta = \zeta_0 + \phi^2 - 2 \cdot \phi \tag{4.9}$$

With another definition of the coefficient of loss, as well as the contraction number and the relative free hole area the pressure loss for the plate can be calculated.

$$\zeta = (\frac{1}{\alpha} - 1)^2 + (1 - \phi)^2 \tag{4.10}$$

$$\phi = \frac{A_h}{A} \tag{4.11}$$

$$\phi = \frac{w}{w_h} \tag{4.12}$$

$$\alpha = \frac{A_e}{A_h} \tag{4.13}$$

$$\alpha = \frac{w_h}{w_e} \tag{4.14}$$

The only variable in this calculation is the superficial velocity. The other parameters depend on the geometry or the properties of the media.

4.3.3. Comparison of calculated and measured data

To proof the measured data it was first compared to the calculated data. The pressure drop of the perforated plate and of the packing were calculated separately and processed according to equation 4.4.

Figure 4.4 shows the difference between the calculated and measured data. The real pressure loss is higher then predicted because of the missing free stream conditions after the perforated plate. Balls prevent the flow of air after the holes by blocking or redirecting the

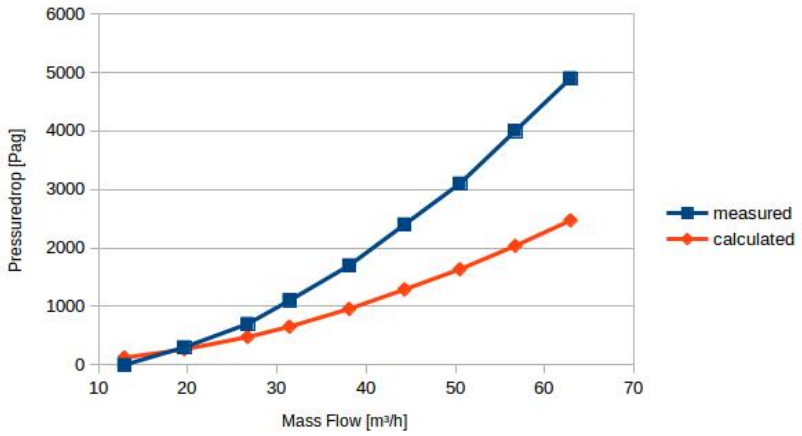

Figure 4.4.: Comparison of the dry pressure drop over the column

gas. Another point that influences the calculated pressure loss is the packing. The pressure loss in it is calculated on the based on an infinitely big packing with a constant porosity over the whole area. The results fit more when the size of the packed bed is increased. In our case the column is very small and and a low ratio between the particle diameter and the column cross section occurs. The wall effects affect the packing much more than in a bigger column.

4.4. Measuring Orifice

The air volume flow rate was measured with a gas meter on the dry bed. There was no water sprinkling. The gas flow increases linearly by increasing the power of the frequency inverter.

The measurement was done until 25 % of the frequency inverter was achieved. This was the limit of the gas meter. The trend of the measurements was linear. To compare higher values the function was extrapolated.

The massflow was calculated as mentioned in standard EN ISO 5167-2.

$$q_m = \frac{C}{\sqrt{1-\beta^4}} \varepsilon \frac{\pi}{4} d^2 \sqrt{2\Delta p \rho_1} \tag{4.15}$$

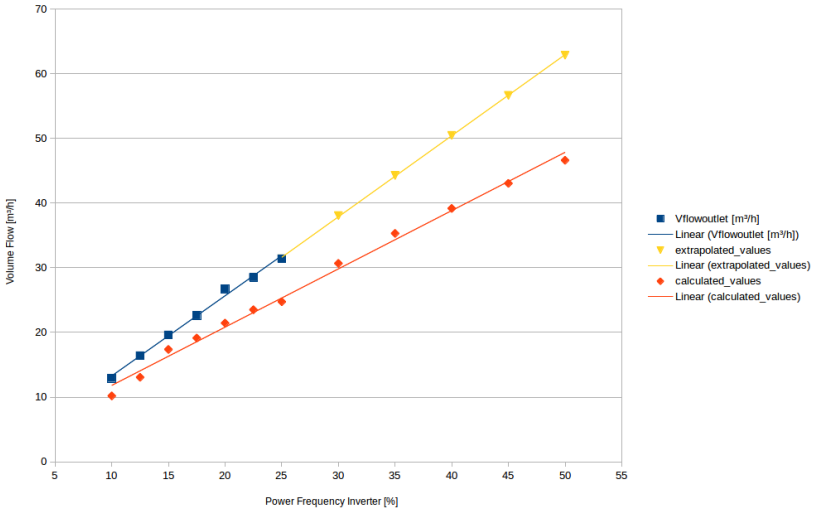

Figure 4.5.: Comparison of the calculated and measured volume flow

β desribes the ratio between the diameter of the measuring orifice and the hole of the orifice. The calculation of C and ε can be seen in the standard.

In figure 4.5 the calculated and the measured volume flow rates are shown. The difference between these two functions increases by increasing the power of the blower. The difference between the measured and the calculated values can be displayed in equation 4.16. This offset must be added to the calculated air volume to determine the real air volumeflow through the packing. X describes the power in % of the frequency inverter.

$$f(x) = 0.3386x - 1,915 \tag{4.16}$$

4.5. Hold up

In case of the setup with table tennis balls, the internal hold up is not considered. The fluid flows directly through the packing without any internal hold up interaction. A pulse of a tracer solution, with a higher conductivity as the tab water, was injected to the fluid phase in top of the column and the response conductivity was measured at the bottom of the packing. Dissolved sodium sulfate was used as tracer. The recorded data showed a residence time distribution, which was used to determine the axial dispersion coefficient, the average velocity and the Bodenstein number.

To get an impression of the change of the conductivity by adding Na_2SO_4 to the tap water a small experimental setup was built (figure 4.6(b)). For this experiments the conductivity of tap water was measured. At each step 0.3 g/l Na_2SO_4 were added to one liter of tap water and the resulting conductivity was recorded. After adding seven gram of sodium sulfate we stopped the experiment. In figure 4.7 the trend of the conductivity and the concentration are shown.

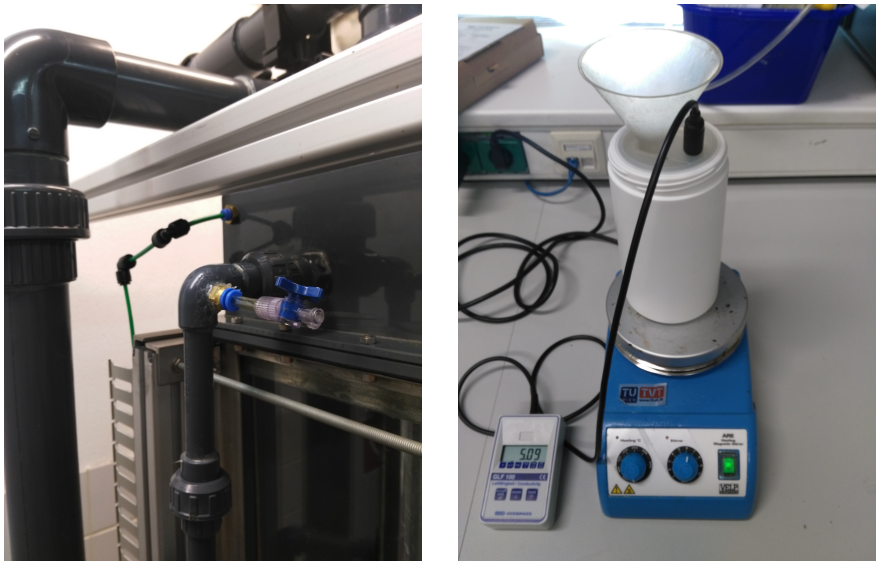

(a) Injectionpoint at the top of the column

(b) Setup up for measuring conductivity

Figure 4.6.: Injection point and setup for conductivity calibration

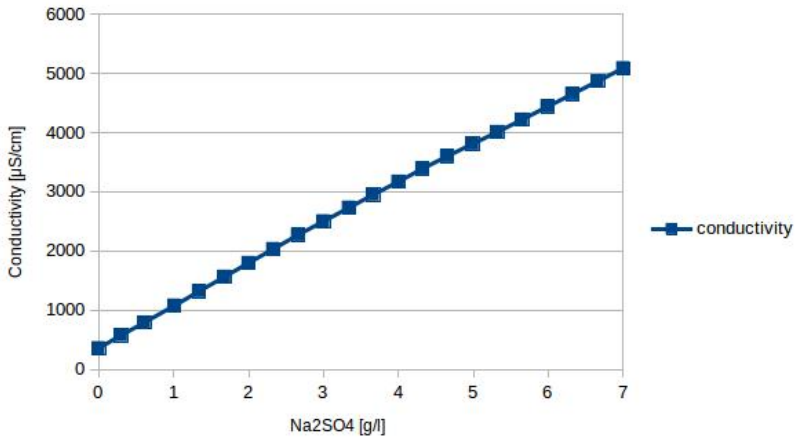

Figure 4.7.: Measured conductivity of Water with Na_2SO_4

A pulse of five ml tracer solution, water with sodium sulfate, was added at the top of the column and the time until the conductivity increases on at the bottom of the trickle bed was measured. During the first attempt a $Na_2SO_4.10H_2O$ solution with 7 g $Na_2SO_4.10$ per liter was used. The result showed, that the conductivity increased not as much as expected after injecting the solution. To increase the changes of conductivity at the bottom of the column a higher amount of sodium sulfate was used. The next solution was prepared with 29 g $Na_2SO_4.10H_2O$ per liter to provide more conclusive values for the conductivity. The injected amount of the tracer solution stayed constant. The injection time was held as short as possible.

The experiment was conducted with a water flowrate of 100 l/h, 175 l/h and 250 l/h. The extra 5 ml of the tracer solution added to the volume flow were ignored in the calculation.

To get the holdup of the packing the delay time from the injection point to the top of the packing was calculated. As mentioned before the water flowrate was 100 l/h, 175 l/h and 250 l/h. The inner diameter of the pipe which distributes the water on the top of the packing is 13 mm. The speed of the water arises from the flow and the area of the pipe which lead to the water distributor.

$$v_{\text{water, 250 l/h}} = \frac{\dot{V}}{A_{\text{pipe}}} = 0.52\frac{m}{s} \tag{4.17}$$

The distance from the injection point to the tip of the distributor is 119.2 cm. With the calculated velocity in equation 4.17 the delay for the highest water flow rate was calculated as 2.28 seconds for 250 l/h. Similarly the time delays for the two other flow rates were calculated.

A stopwatch was used to fit the results for each timestep to the belonging conductivity.The stopwatch was started at the same moment as the tracer was injected. The experiment was done with five different air flow rates between 12.9 m^3/h and 38.1 m^3/h at three different water flow rates. To get vertices of the experimental setup the water flow rate of 50 l/h at 12.9 m^3/h and 38.1 m^3/h air flow were evaluated as well. The duration of each of the experiments was approximately one to two minutes. After this time the conductivity was equal to the starting level of the conductivity.

In figure **??** all accomplished holdup experiments are shown. With these points the hold up of the absorption column can be evaluated. For all experiment the air flow rates were kept constant. This could be measured with the pressure sensors on the experimental setup. The

water flow was not 100 % stable at low flow rates and was adjusted during the experimental runs.

To analyze the behavior of the column the tracer was injected on the top and the conductivity was measured after the packing on the perforated plate. The stopwatch and the conductivity measurement tool were being filmed during the whole experiment. This data was transferred to a data evaluation tool. Every second the associated conductivity was recorded.

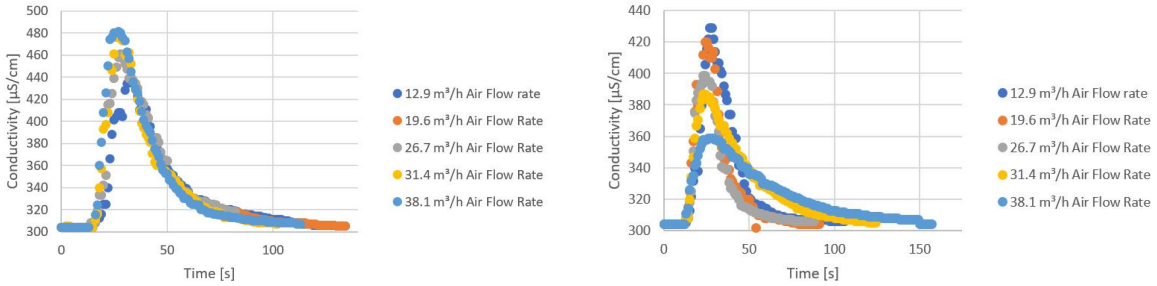

(a) Conductivity at 100l/h water flow Rate

(b) Conductivity at 175l/h water flow Rate

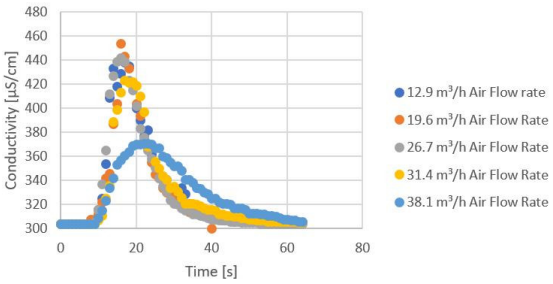

(c) Conductivity at 250l/h water flow Rate

Figure 4.8.: Results of the conductivity measurement

Figure 4.8 shows the results of the experiment with three different water flow rates. From these pictures it is already possible to draw the first conclusions. The water flow rate of 100 l/h shows just little differences of the conductivity distribution at the gas flow rates. At 250 l/h the shortest residence time of all three experiments can be seen. At high gas flow rates the water is better distributed in the trickle bed. The graph gets wider. The best differences between the gas flow rates shows graph 4.8(b). It can also be mentioned that the average residence time is not dependent on the gas flow rates. This can be estimated from the peaks of the single graphs. The peaks do not differ much from each other. A quite constant residence time can be expected . This behavior was also analyzed by A. Bittante 2014

[Bittante et al., 2014]. Figure 4.9 shows the average residence time is just dependent on the water flow rate. The residence time increases the lower the water flow rate is.

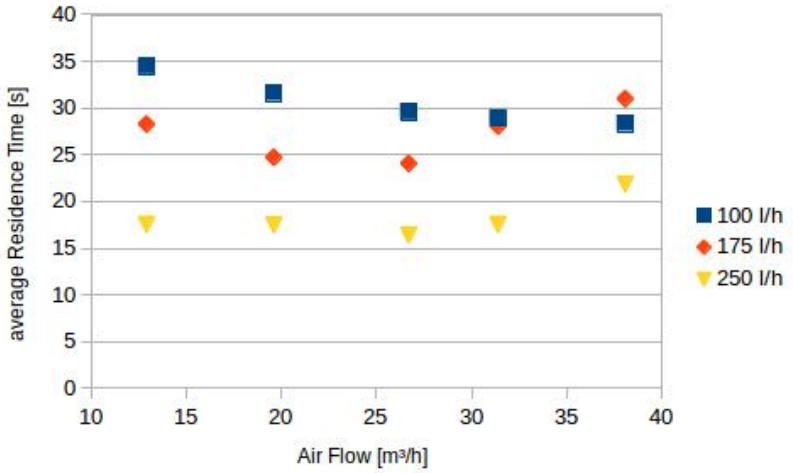

Figure 4.9.: Comparison of the average residence times

The average residence time was calculated with the approach of Levenspiel in chapter 2.3.5 and is explained later. The experimental evaluated values for the conductivity and the associated concentrations were used for the following results. The starting conductivities of the experiments depend on the day they were made. Every day the water had a different conductivity. That could been seen in the results. To get a proper value for all measurements the day with the lowest conductivity was chosen as a basis for the calculation. The other values have been fitted with an offset to the base value and got converted to the associated conductivity.

To get an impression of the behavior of the water in the trickle bed the approach of Levenspiel [Levenspiel and Smith, 1957], equation 2.81, was chosen. With this distribution function the axial dispersion coefficient and the average residence time could be evaluated. To get comparable results the time was normalized to the dimensionless time and the concentration remodeled to the base of the concentration in the tracer. A least squared analysis was used to evaluate the smallest deviation of the actual concentration of the experiment and the calculated values of the distribution equation of Levenspiel. The values of the average residence time and the dispersion coefficient were changed via Microsoft Excel until the lowest difference between the experimental data and the calculated data occurred. To confirm the results the integral of this distribution was calculated numerically. Because the points

had been measured every second it is a good way to approximate this integral to sum up all concentration values. The integral of a distribution function from zero to infinity always has to equal one. The results for our experiments are all approximately one. The biggest difference was twenty percent, but only occurred once. Other deviations were between five and ten percent. The reason for this were measuring errors and inaccuracies of the measurement tool. Nevertheless this comparison shows good matches of both distributions. The average residence times can be seen in figure 4.9.

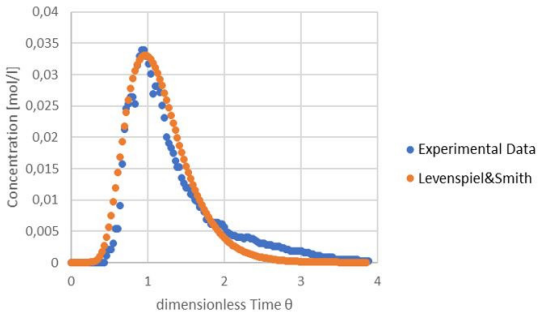

(a) Air flow rate 12.9 m^3/h

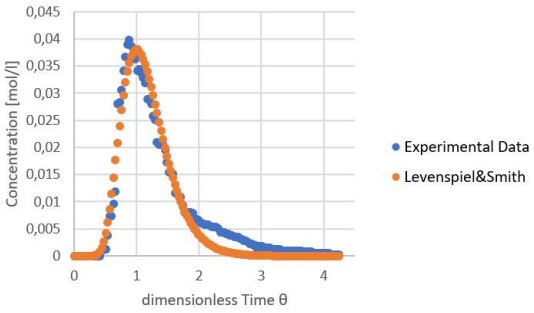

(b) Air flow rate 19.6 m^3/h

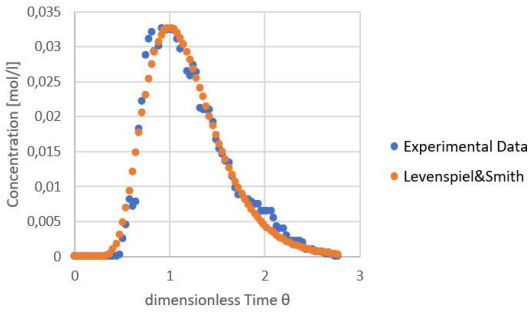

(c) Air flow rate 26.7 m^3/h

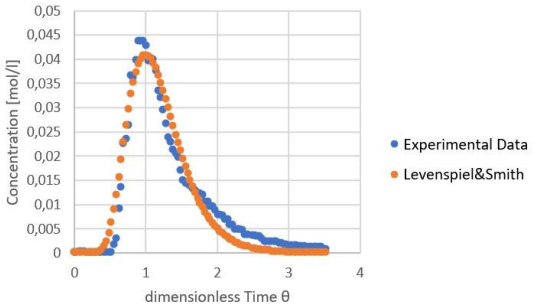

(d) Air flow rate 31.4 m^3/h

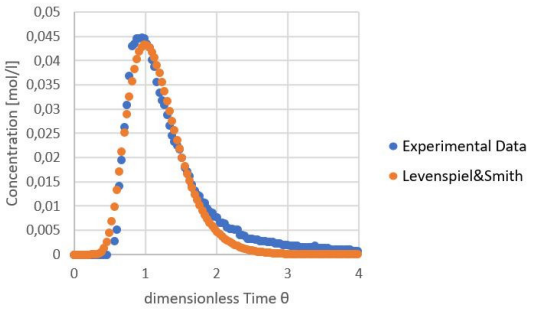

(e) Air flow rate 38.1 m^3/h

Figure 4.10.: Experimental conductivity at 100 l/h water flow rate

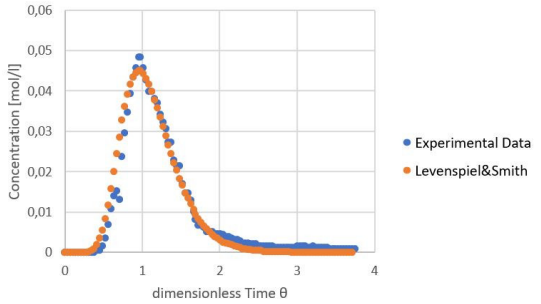

(a) Air flow rate 12.9 m^3/h

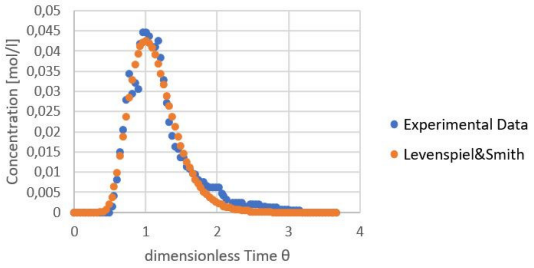

(b) Air flow rate 19.6 m^3/h

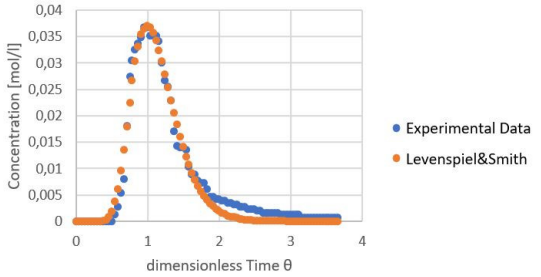

(c) Air flow rate 26.7 m^3/h

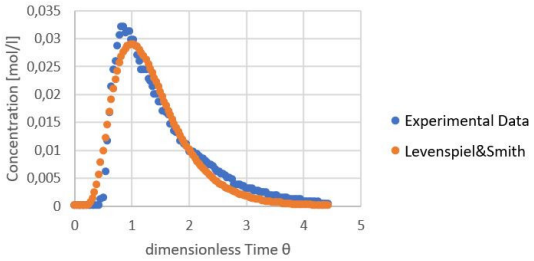

(d) Air flow rate 31.4 m^3/h

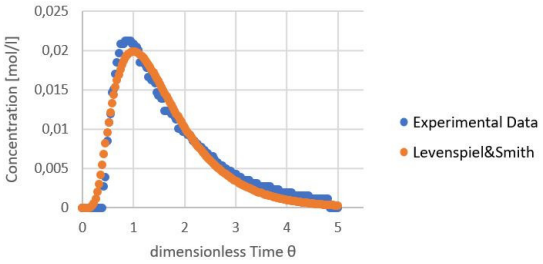

(e) Air flow rate 38.1 m^3/h

Figure 4.11.: Experimental conductivity at 175 l/h water flow rate

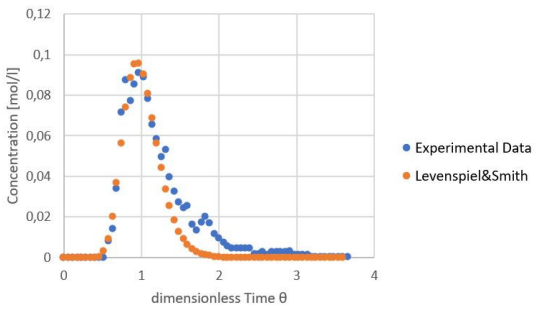

(a) Air Flowrate 12.9 m^3/h

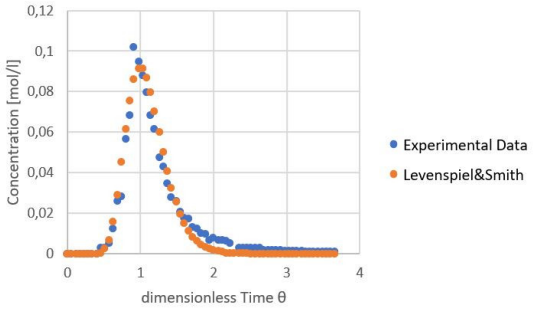

(b) Air Flowrate 19.6 m^3/h

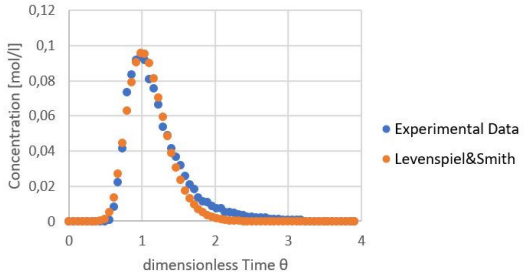

(c) Air Flowrate 26.7 m^3/h

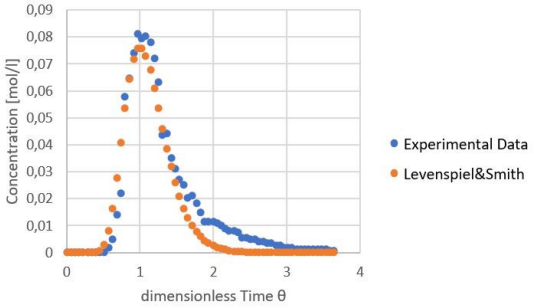

(d) Air Flowrate 31.4 m^3/h

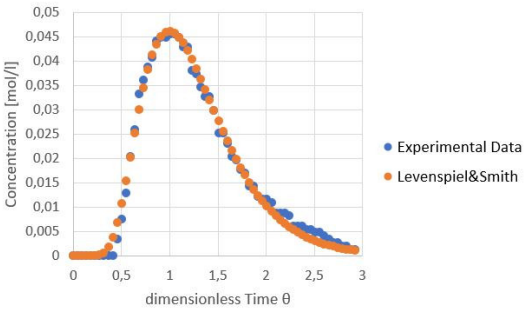

(e) Air Flowrate 38.1 m^3/h

Figure 4.12.: Experimental conductivity at 250 l/h water flow rate

The axial dispersion of the water phase and the average residence time can be calculated by the approximation of Levenspiel 2.81. The average velocity of the liquid phase was calculated with the average residence time and the height of the packing.

The Bodenstein number is a benchmark for axial dispersion of the liquid phase in a trickle bed. As seen in equation 2.78 this dimensionless number is dependent on the velocity of the

water trickle down the packing, the height of the packed bed and the dispersion coefficient. The water velocity in the packing depends on many factors: the air flow limit ,the space where the water is able to flow down through the packing on the surface film on the particles. It must also be mentioned that the air outlets are arranged in a circle on the perforated plate. This also influences the water flow. The water distribution on top the packing is an important parameter for the Bodenstein number. During the high water flow rates of 250 l/h the waterjet reaches a larger area on the top of the packing. At 100 l/h the water just trickles from the tip of the water distribution unit.

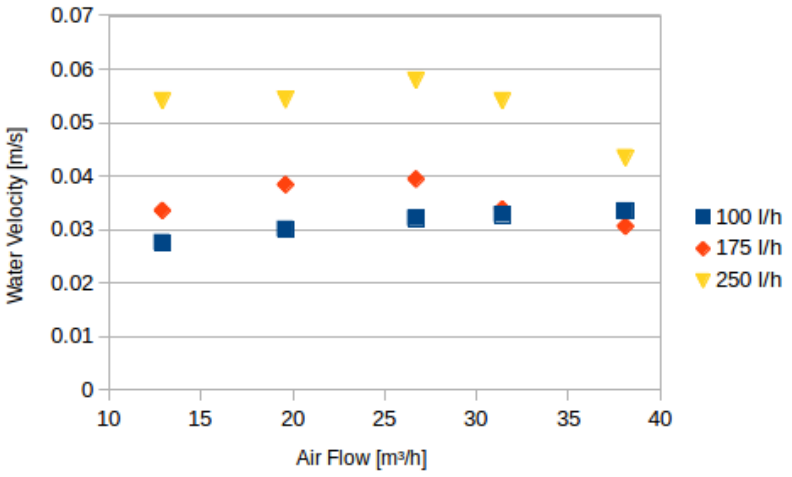

Figure 4.13.: average Velocity of the water in the packing

For the water flow rate of 250 l/h a tendency is apparent. At an air flow rate of 26.7 m^3/h the velocity starts decreasing. A similar trend can be seen at 175 l/h. The low water flow rate of 100 l/h shows a constantly increasing progression of the water flow rates. It seems that the lower air flow rates up to 26.7 m^3/h have no effect on the velocity of the two water flow rates of 175 l/h and 250 l/h. The higher air flow rates distribute the water over the packing and the average velocity drops. The increased average water velocities for the low water flow rate can be explained by the lesser space, which was taken by the air flow, the water has to trickle down the packing. The calculated dispersion coefficient was also compared in figure 4.14.

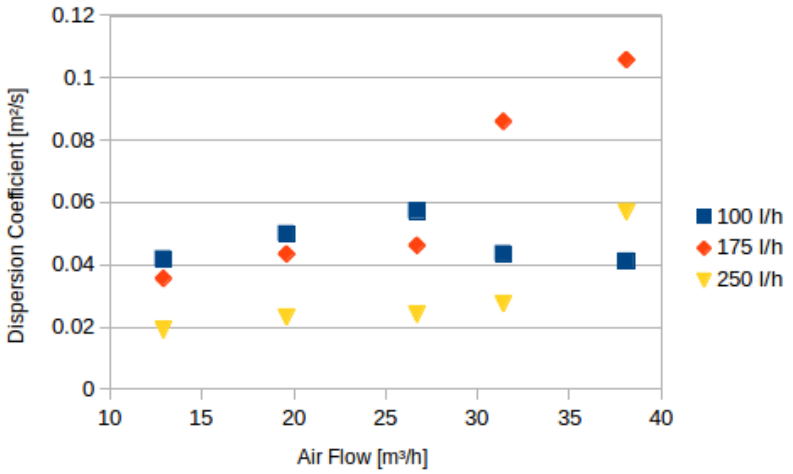

Figure 4.14.: Dispersion coefficient at different air flow rates

Similar behaviors for higher water flow rates can be seen. Both trends increase with higher air flow rates. Again at an air flow rate of 26.7 m^3/h the dispersion coefficient increases faster than at lower gas flow rates. An opposite picture merges for the low water flow rate of 100 l/h. The dispersion coefficient decreases after the mentioned air flow rate. As mentioned in the section 2.3.5 a higher Bodenstein number indicates that the flow behaves more like plug flow. The lower the value gets, the more it corresponds to a full backmixing.

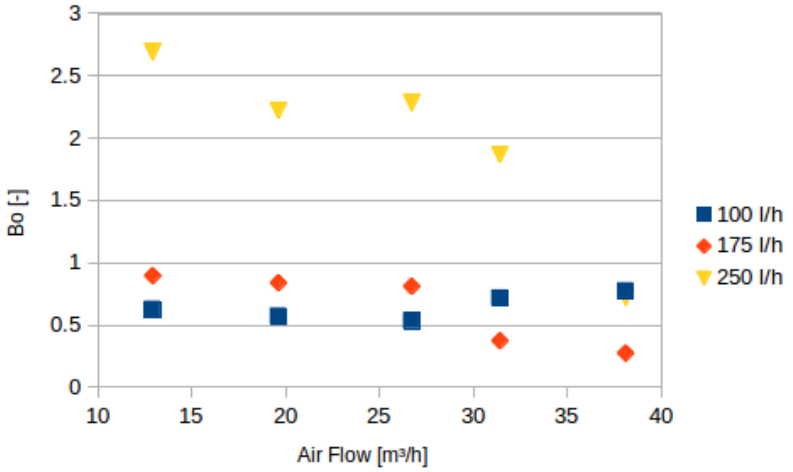

Figure 4.15.: Bodenstein number at different water flow rates

As seen in figure 4.15 the results of the water flow rate 100 l/h stays almost constant for all air

flow rates. This result was unexpected. Indeed it is always a low Bodenstein number ,which means that a good mixing process takes place, but the mixing process does not improve with higher air flow rates. This phenomenon can be explained by the circularly arranged air holes in the perforated plate and the central water distribution on the top of the packed bed. The water trickles down the packed bed just in the center of it. The air flow surrounded this water flow and prevented it from getting to all areas of the packing. The two other water flow rates show similar behavior. A nearly constant Bodenstein number starts droping after an air flow rate of 26.7 m^3/h. This trend is more extreme at the highest water flow rate of 250 l/h. The Bodenstein number drops at the highest air flow rate under the determined Bodenstein number of water flow rate of 100 l/h. This result means that the highest change of mixing occurred in this range. The highest back mixing behavior can be found with a water flow rate 175 l/h and the highest air flow rates.

The evaluated values have been compared to the correlations in chapter 2.3.5. The correlations show a rough idea of the expected values, however these approaches have some limiting factors.

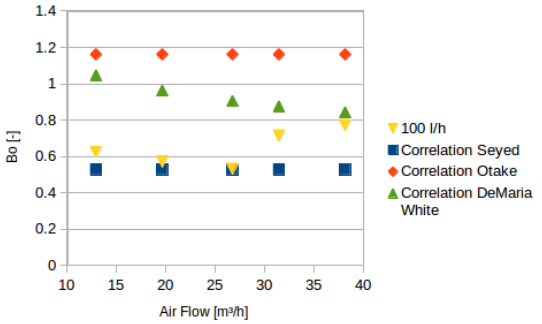

(a) Correlations at 100l/h Water Flow Rate

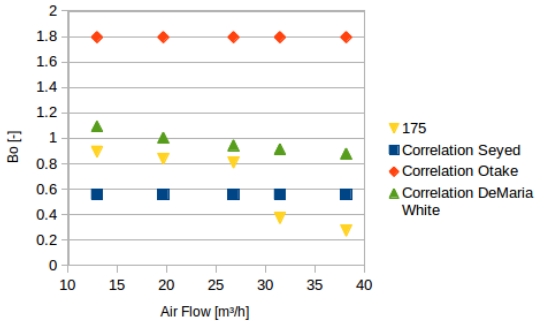

(b) Correlations at 175l/h Water Flow Rate

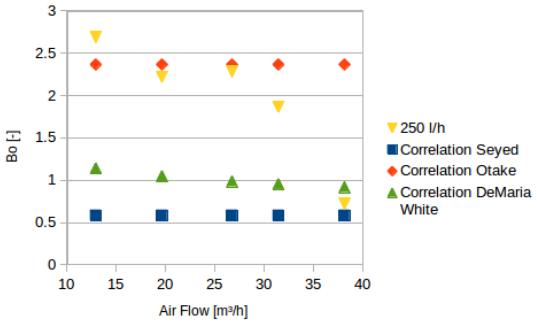

(c) Correlations at 250l/h Water Flow Rate

Figure 4.16.: Comparison of Correlations at different Water Flow Rates

In figure 4.16 the different approaches have been compared to the experimental data. In case of this experimental setup different correlations fit better for different areas. The biggest problem of the correlations of Seyed and Otake is the independency of the air flow rate. The estimated values stay constant over the whole range. Nevertheless a trend of the Bodenstein number can be estimated. Especially for the two lower water flow rates, 100 l/h and 175 l/h, the correlations of Seyed and the one of Demaria and White deliver good limits for the experimentally evaluated Bodenstein number. For the water flow rate of 100 l/h the correlation of Seyed can be used for the low air flow rates from 12.9 m^3/h to 26.7 m^3/h. The other two values can be better estimated by the correlation of Demaria and White. The opposite effect is true for the water flow rate of 175 l/h. The approach of Demaria and White works better for the lower air flow rates and the concept of Seyed is more suitable the higher flow rates. At lower water flow rates the correlation of Otake is cannot be taken. The evaluated values are much too high. At a water flow rate of 250 l/h the approximation of Otake fits well for the first few air flow rates. As already mentioned this approach does not account of the air flow rates. At high air flow rates the Bodenstein number drops. At this point the correlation of Otake does not no longer work. At the highest air flow rate of 38.1 m^3/h the estimations of Demaria and Seyed fit the experimentally determined value.

The evaluated results can be seen in the tables 4.1 - 4.6

Air Flow rates	peak time [s]	average residence time [s]	average water velocity [m/s]	dispersion coefficent [m^2/s]	Bodenstein number [-]
12.9 m^3/h	32	34.46	0.028	0.042	0.63
19.6 m^3/h	28	31.6	0.03	0.05	0.57
26.7 m^3/h	27	29.58	0.032	0.057	0.53
31.4 m^3/h	27	28.95	0.033	0.044	0.72
38.1 m^3/h	27	28.36	0.033	0.041	0.77

Table 4.1.: Determined parameter for 100 l/h water flow rate

Air Flow rates	peak time [s]	average residence time [s]	average water velocity [m/s]	dispersion coefficent [m^2/s]	Bodenstein number [-]
12.9 m^3/h	27	28.29	0.034	0.036	0.9
19.6 m^3/h	24	24.73	0.038	0.043	0.84
26.7 m^3/h	24	24.08	0.039	0.046	0.81
31.4 m^3/h	24	28.06	0.034	0.086	0.37
38.1 m^3/h	27	31.01	0.031	0.106	0.27

Table 4.2.: Determined parameter for 175 l/h water flow rate

Air Flow rates	peak time [s]	average residence time [s]	average water velocity [m/s]	dispersion coefficent [m^2/s]	Bodenstein number [-]
12.9 m^3/h	17	17.55	0.054	0.019	2.69
19.6 m^3/h	16	17.49	0.054	0.023	2.22
26.7 m^3/h	16	16.4	0.058	0.024	2.28
31.4 m^3/h	19	17.55	0.054	0.027	1.87
38.1 m^3/h	22	21.86	0.043	0.057	0.72

Table 4.3.: Determined parameter for 250 l/h water flow rate

Air Flow rates	Bo experimental [-]	Bo Seyed [-]	Bo Otake [-]	Bo DeMaria and White [-]
12.9 m^3/h	0.63	0.53	1.16	1.05
19.6 m^3/h	0.57	0.53	1.16	0.96
26.7 m^3/h	0.53	0.53	1.16	0.9
31.4 m^3/h	0.72	0.53	1.16	0.88
38.1 m^3/h	0.77	0.53	1.16	0.84

Table 4.4.: Evaluated Bodenstein numbers for 100 l/h water flow rate

Air Flow rates	Bo experimental [-]	Bo Seyed [-]	Bo Otake [-]	Bo DeMaria and White [-]
12.9 m^3/h	0.9	0.56	1.79	1.09
19.6 m^3/h	0.84	0.56	1.79	1
26.7 m^3/h	0.81	0.56	1.79	0.94
31.4 m^3/h	0.37	0.56	1.79	0.91
38.1 m^3/h	0.27	0.56	1.79	0.88

Table 4.5.: Evaluated Bodenstein numbers for 175 l/h water flow rate

Air Flow rates	Bo experimental [-]	Bo Seyed [-]	Bo Otake [-]	Bo DeMaria and White [-]
12.9 m^3/h	2.69	0.58	2.37	1.14
19.6 m^3/h	2.22	0.58	2.37	1.05
26.7 m^3/h	2.28	0.58	2.37	0.99
31.4 m^3/h	1.87	0.58	2.37	0.95
38.1 m^3/h	0.72	0.58	2.37	0.92

Table 4.6.: Evaluated Bodenstein numbers for 250 l/h water flow rate

4.6. Mass Transfer

4.6.1. Expected Mass Transfer for Oxygen

In order to estimate how much Oxygen is expected in the gas and liquid phase a mass balance for oxygen was used. In this case the temperature of the air and water were $22°C$. In this case air has a density of $\rho = 1,2041 \frac{kg}{m^3}$. In case of 75,51 % of mass the density of oxygen in the air is $0,278749 \frac{kg}{m^3}$. For our calculation the same balance was used as seen in figure 2.7. In the optimal case, when water is saturated with 8,53 mg/l oxygen from zero to its equilibrium at $22°C$ with a maximum of highest measurable water flow rate is 320 l/h, the lowest air flow rate, which the blower can provide stable of 12,9 m^3/h. In this case 12,7 mg/l O_2 are dissolved.

4.6.2. Dissolved Oxygen Measurement

For measuring the dissolved oxygen in the liquid and in the gas phase, four devices were used. For the gas phase the inlet was measured before entering the sump of the column and the outlet on the top before the gas exited the absorber. On the liquid side the input concentration of the dissolved oxygen was determined in the water storage tank. The saturated water is measured at the bottom of the packing at the new perforated plate. For measuring the dissolved oxygen in different phases three different types of measurement devices of two different manufactures were used.

- Greisinger GMH 3630 for air (2x)
- Greisinger GMH 3610 for dissolved O_2 water
- Voltcraft DO-100 for dissolved O_2 water

For testing the devices a small setup (figure 4.17) was created. In this setup one liter of water was flushed with nitrogen - oxygen mixture with oxygen volume fraction from 0% to 25%. The 0_2 concentration was measured in the water, which had been mixed with a magnetic stirrer, and in the gas feed. After each increase of the oxygen volume fraction the measured values at the steady state had been recorded.

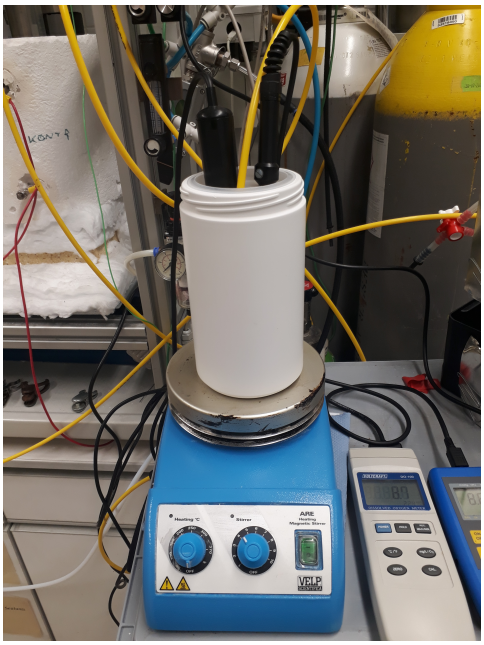

Figure 4.17.: Experimental setup for oxygenmeasurement

The results of the measurements revealed some unexpected problems with the O_2 probes. The two different measuring units for dissolved oxygen in liquid produced different values at all points. The tests were repeated multiple times, but the results varied for each experiment.

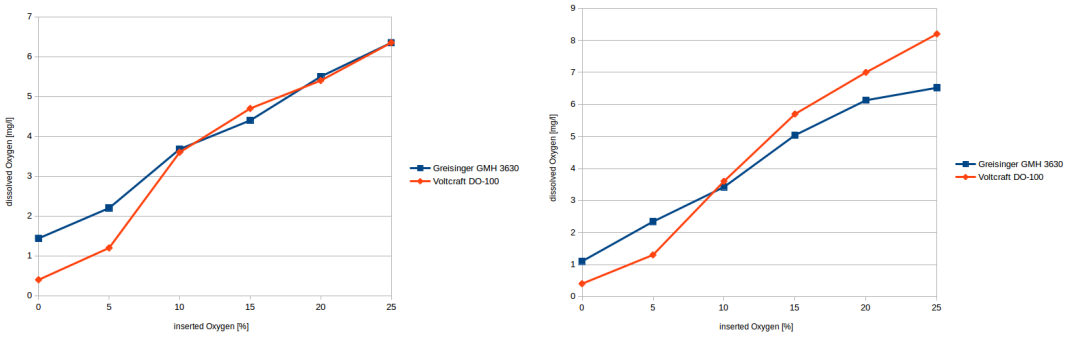

(a) Results Experiment 5 (b) Results Experiment 7

Figure 4.18.: Values for dissolved oxygen in water

The measurement were done seven times producing seven different results. In figure 4.18 experiment number four and number seven are compared. These two cases show the biggest differences of all experiments. Not only do the graphs show differing values, but also different behaviors. The reason for this measurements may occur because of the bad mixing of the magnetic stirrer. Further experiments showed fitting values between those two sensors in a more turbulent ambient.

To see if the measurements for this fit two gas sensors were added to the experimental setup. The gas measurements delivered more promising values. A sample comparison of the experimental runs on the gas side can be observed in figure 4.19. The results of all experiments can be seen in appendix B.

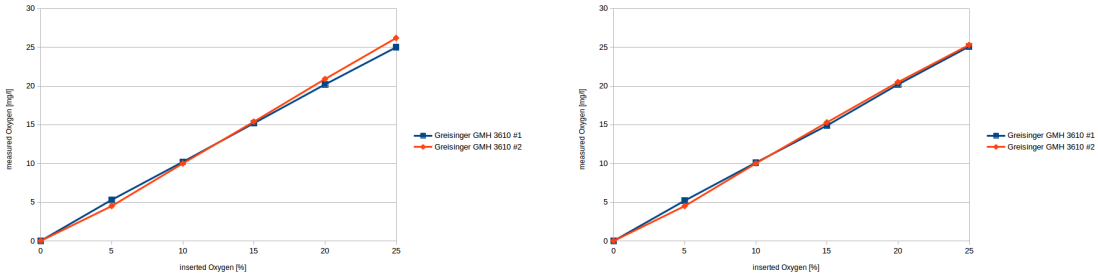

(a) Results Experiment 6 (b) Results Experiment 7

Figure 4.19.: Values for oxygen in air

4.6.3. Mass Transfer Experiments

For the experiment the water tank was flushed with nitrogen to reduce the amount of oxygen in the water. This operation was measured with both saturated oxygen devices. As expected the values of both measuring devices differed from each other. While the Voltcraft DO-100, which will stayed in the tank, showed 0.4 mg O_2/l the Greisinger GMH 3630 showed 2.08 mgO_2/l. The Greisinger measurement tool stayed at the bottom of the perforated plate.

The water flow rate was 250 l/h and the air flow rate 12.9 m^3/h. During the experiments the tank was still flushed with nitrogen to keep the oxygen level in the tank constant. The oxygen sensors for the gas side were not calibrated. The different pressures at the bottom and top of the column were not considered and the values of these measurement devices are not considered. The value of the "saturated" water at the bottom of the column was 7.46 mg O_2/l at a steady state. This contrasts the starting value of 5.38 mg O_2/l in the packing.

On another day two further experiments were conducted. In them the highest and lowest air- and water flow rates were paired together. During this test run the oxygen sensors for air were calibrated correctly and set to the right pressure at each position. The objective of measuring the oxygen on the liquid and on the air side was to get more values to calculate the mass transfer for both phases. The experiments were conducted with two combinations:

- High water flow rate of 250 l/h and low air flow rate of 12.9 m^3/h
- Low water flow rate of 100 l/h and a high air flow rate of 38.1 m^3/h

With these experiments two very different results of the final oxygen saturation and the oxygen mass transfer were expected. For the second experimental run the tank was flushed with nitrogen again until the amount of dissolved oxygen in the water reached one mg O_2/l water. With one filling of the water tank both experiments were conducted.

For the first experimental run, with the high water- and the low air flow rate, the blower and the pumps were started. The pressure in the bottom and top of the column were measured by the pressure sensors. The oxygen sensors for the gas phase were calibrated for this values. The absorption column was operating until a steady state was reached. This procedure was followed during the second experiment as well.

The results for these experiments were unexpected. At both experiments produced nearly the same values. The experiment with the low air flow rate of 12.9 m^3/h and the high water

flow rate of 250 l/h managed a saturation of 5.05 mg O_2 per liter of water. This value was similar to the first experiment a few days before. The other experimental run with the high air flow rate of 38.1 m^3/h and the low water flow rate of 100 l/h a dissolved oxygen value of 5,25 appeared. In case of a measuring error of about 10 percent both values can be deducted as the same. From this results it can be seen that independent of the flow conditions of water and air the same amount of oxygen is transfered between both phases appear in the packing. The solution to solve this problem is a longer packing with a bigger residence time and a better dispersion of the water in the trickle bed. Adding pure oxygen to the air flow will also influence the results of these experiments.

Water flow rate [l/h]	Air flow rate [m^3]	dissolved O_2 tank [mg/l]	dissolved O_2 bottom [mg/l]	ΔO_2 [mg/l]
250	12.9	2.08	7.46	5.38
250	12.9	0.7	5.75	5.05
100	38.1	0.7	5.95	5.25

Table 4.7.: O_2 transfer of all experiments

Evaluated dimensionless numbers

The most of the mentioned dimensionless numbers, in chapter 2.3.4, have been evaluated for the experimental parameter. Because of the dependency on the temperature of some parameters a steady temperature of 20 °C has been chosen. The superficial velocity was calculated dependent on the cross section of the column and can be seen in table 4.8 and table 4.9.

Airflow Rate	superficial Velocity [m/s]
12.9 m^3/h	0.094
19.6 m^3/h	0.143
26.7 m^3/h	0.195
31.4 m^3/h	0.229
38.1 m^3/h	0.278

Table 4.8.: Superficial velocity of air

Waterflow Rate	superficial Velocity [m/s]
100 l/h	0.000731
175 l/h	0.001278
250 l/h	0.001826

Table 4.9.: Superficial velocity of water

The physical conditions for the used media, water and air, are shown in table 4.10.

	Air	Water
Density [kg/m^3]	1.188	998.21
Viscosity [Pas]	1.824E-5	1.002E-3
Diffusioncoefficient O2 [m^2/s]	1.75E-5	2.1E-9
Surface tension [N/m]	-	0.07275

Table 4.10.: Physical parameter for the phases

The settings of the geometrical properties used for this calculations are shown in table 4.11.

Particle diameter [m]	0.037263
Column diameter [m]	0.195
Porosity [-]	0.4
a_x [m^2/m^3]	117.12

Table 4.11.: Geometrical properties of the packing and column

In this table ax defines the external area of particles and wall per unit of reactor volume. This parameter is defined by equation 4.18. Φ describes the sphericity factor. For this case, table tennis balls, a factor of one was chosen. For the column diameter, d_c, the edge length of the column was chosen.

$$a_x = 6\frac{(1-\varepsilon)}{\Phi d_P} + \frac{4}{d_c} \tag{4.18}$$

With this parameter the dimensionless numbers can be calculated for the liquid (table 4.13) and the gas phase (4.12).

Airflow Rate	**Reynolds Number**	**Weber Number**	**Schmidt Number**
12.9 m^3/h	228.71	4.54	0.88
19.6 m^3/h	347.5	10.48	0.88
26.7 m^3/h	473.38	19.45	0.88
31.4 m^3/h	556.71	26.9	0.88
38.1 m^3/h	675.5	39.61	0.88

Table 4.12.: Dimensionless numbers for the gas phase

Waterflow Rate	**Reynolds Number**	**Weber Number**	**Schmidt Number**
100 l/h	27.12	4.54	478
175 l/h	47.46	10.48	478
250 l/h	67.8	19.45	478

Table 4.13.: Dimensionless numbers for the liquid phase

Waterflow Rate Airflow Rate	100 l/h	175 l/h	250 l/h
12.9 m^3/h	4.45	2.54	1.78
19.6 m^3/h	6.76	3.86	2.7
26.7 m^3/h	9.21	5.26	3.68
31.4 m^3/h	10.83	6.19	4.33
38.1 m^3/h	13.14	7.51	5.26

Table 4.14.: Lockhart Martinelli Number dependent on air- and waterflow

With the calculated dimensionless numbers the Sherwood number out of the correlation of White out of the scientific paper of Iliuta ([Iliuta et al., 1999]) could be evaluated. For further investigations the correlation of high interaction of the liquid phase should be considered. The correlations for the low interaction and the transition regime deliver way to huge Sherwood numbers.

Waterflow Rate Airflow Rate	100 l/h	175 l/h	250 l/h
12.9 m^3/h	9803.9	9814.4	5404.3
19.6 m^3/h	12867.2	8943.5	7092.9
26.7 m^3/h	15730.7	10933.9	8671.4
31.4 m^3/h	17479.2	12149.2	9635.2
38.1 m^3/h	19820.6	13776.6	10925.9

Table 4.15.: Sherwood number for high interaction

Chapter 5.

Simulation

Selected experiments on the absorption column are simulated in CFD. Computational fluid dynamics describes a way to solve fluid dynamic problems numerically with the help of software, which cannot be solved analytically.

The procedure to solve such a numerical problem has a defined order [Spurk and Aksel, 2007].

1. Problem definition
2. Selection of the physical models and the used numerical equations
3. Creating of a geometry
4. Discretization of the prepared CAD model
5. Numerical solution via Computational Fluid Dynamics
6. Post processing of the evaluated data

For the calculation of such numerical problems differential equations are used. The base equations are the continuity equation (equation 5.1), the energy equation (equation 5.2) and the momentum equation also known as Navier-Stokes equation (equation 5.3).

$$\frac{\partial \rho}{\partial t} + \frac{\partial \rho u}{\partial x} + \frac{\partial \rho v}{\partial y} + \frac{\partial \rho w}{\partial z} = 0 \tag{5.1}$$

$$\frac{\partial \rho c_v T}{\partial t} + u\frac{\partial \rho c_v T}{\partial x} + v\frac{\partial \rho c_v T}{\partial y} + w\frac{\partial \rho c_v T}{\partial z} = -[\frac{\partial q_x}{\partial x} + \frac{\partial q_y}{\partial y} + \frac{\partial q_z}{\partial z}] - T(\frac{\partial P}{\partial T})_\rho(\frac{\partial u}{\partial x} + \frac{\partial v}{\partial y} + \frac{\partial w}{\partial z}) - [\tau_{xx}\frac{\partial u}{\partial x} + \tau_{yy}\frac{\partial v}{\partial y} + \tau_{zz}\frac{\partial w}{\partial z}] - [\tau_{xy}(\frac{\partial u}{\partial y} + \frac{\partial v}{\partial x}) + \tau_{xz}(\frac{\partial u}{\partial z} + \frac{\partial w}{\partial x}) + \tau_{yz}(\frac{\partial v}{\partial z} + \frac{\partial w}{\partial y})] + S_T \tag{5.2}$$

Momentum is a vectorial quantity and must be considered in all three dimensions. The described equation shows just the x-direction of the Navier-Stokes equation.

$$\frac{\partial \rho u}{\partial t} + u\frac{\partial \rho u}{\partial x} + v\frac{\partial \rho u}{\partial y} + w\frac{\partial \rho u}{\partial z} = -\frac{\partial P}{\partial x} - (\frac{\partial \tau_{xx}}{\partial x} + \frac{\partial \tau_{yx}}{\partial y} + \frac{\partial \tau_{zx}}{\partial z}) + \rho g_x + S_u \tag{5.3}$$

To solve these numerical problems a discretization method has to be used. The differential equations get approximated with a system of the algebraic equations. This approximations are used on small areas on a specific place or time [Ferziger, 2002]. There are many different discretization methods, the most important ones are:

- Finite Difference
- Finite Volume
- Finite Elements

In the finite difference method the area is overlapped by a mesh. Each node approximates the differential equations based on the values there. The finite volume method uses the integral form of the conservation equations as base. The area is split up in a finite number of volumes. The finite element method is quite similar to the finite volume method. The equations are just multiplied by a weighted function before they are solved. In this work the finite volume method is used for the numerical calculations.

5.1. Geometry

The geometry for the simulation had to be created. For creating the necessary geometry Autodesk Inventor 2018 was used. The geometry contains the column itself with all its in and outlets, which function as boundaries. For small changes or adaptations for the simulation

FreeCAD was used. Attention must be paid to the consistency and accuracy of the drawing. Otherwise problems with the further steps can occur.

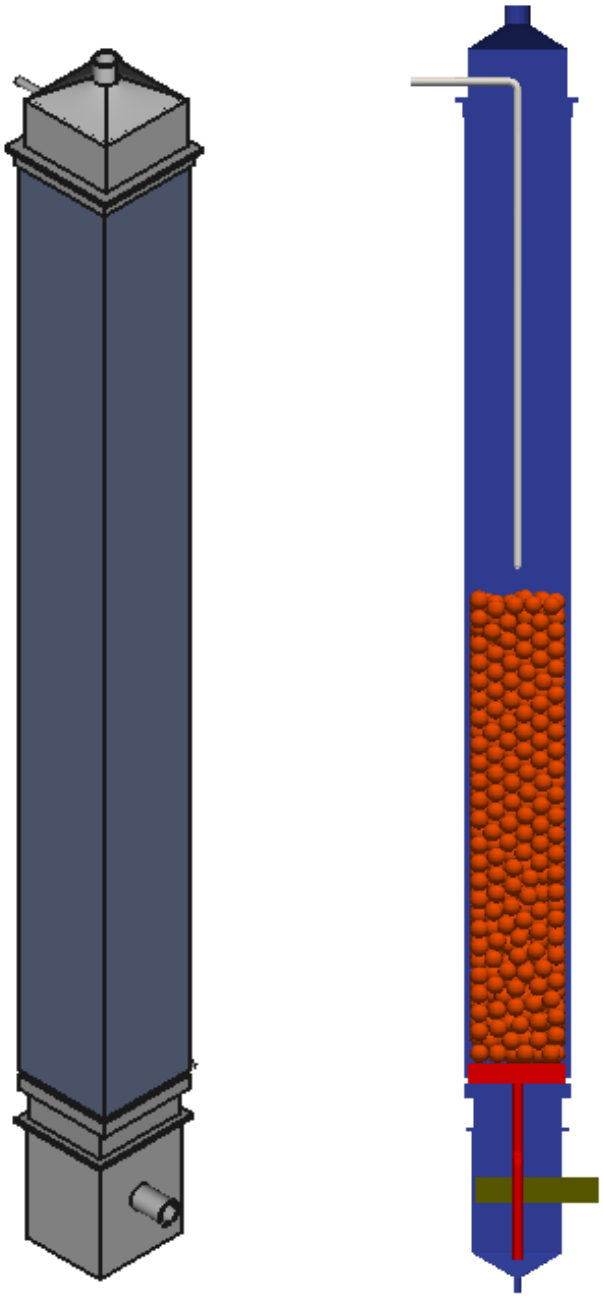

(a) Geometry of the Simulation Setup (b) Inside of the column

Figure 5.1.: Outside and Inside Geometry of the column

For the CFD simulation itself not every single detail had to be modeled. The important part of the geometry is the inside of the column. For that reasons the outer walls were created without any thickness. Also very detailed parts like threads or screws were not included as they have no influence for the flow. The gaps between the parts with their sealings were ignored. The flanges were only modeled using the inner diameter of the equivalent pipe. Not the whole experimental setup was modeled in Autodesk Inventor 2018. The outer parts like the two pumps, the tank and the pipes for air and water, that lead to and off the column were omitted. The boundaries on the in- and outlet of the column were set using the results of the measurement systems. Also the mesh on the top and the bottom of the packing were not considered. The expected influence of the bottom mesh on the flow conditions and the mass transfer is insignificantly small. The same train of thought was used for the mounting of the mesh on the top of the trickle bed. Figure 5.1(b) shows the inside of the column. The outer border of the column is shown in blue. On the top of the column the gas outlet is shown. On the bottom of the column the water outlet can be seen. The grey part, which reaches from the top to the packing is the water distributor. The green pipe which leads to the sump provides the air flow to the setup. On the bottom of the packing, in red, the bottom plate is shown. The pipe from the perforated plate in the sump is also shown in red. The orange ball packing is shown in the middle of the column. The packing was created with a DEM code, that was programmed by the team of Michael Harasek of the TU-Wien. This code places particles, in this case the table tennis balls, in a defined geometry. For this simulation 1000 of these particles were placed in a ten meter high defined geometry with the same base area as the absorption column. The reason for this height was the influence of the particles among each other. The forces between the particles lead to an impetus which delivers the particles out of the defined zone. The used DEM code deletes particles, which are not in the defined geometry automatically. After this DEM solver finished its calculations the packing was cut to the height of the packing of the original setup. The simulation provided 769 particles after the reduction, which is nearly the same as the 774 particles which were used in the experimental setup. With this simulation a stl file for the packing was created and used in the geometry.

Density [kg/m^3]	7700
Young Modulus [MPa]	220
Shear Modulus [MPa]	85.94
Poisson Ratio [-]	0.28
Particle Diameter [m]	0.03726

Table 5.1.: Particle properties for the virtual packing

5.2. Mesh

The used discretization, where the different variables are calculated is defined by a numerical grid. This grid divided the solution area in a finite amount of small regions.

The mesh was created with snappyHexMesh. For this application a background mesh is needed which was created by blockMesh. This background mesh got refined and the unused cells were removed. To refine the cells at the surfaces the cells were snapped to them. In a further, but not necessary step, layers could be added to the surfaces.

The mesh, for the absorption column, which was used for this thesis contained 8.586.191 cells. For this mesh several regions had a finer mesh. The finer mesh was needed especially for all parts with small holes like the distribution units for water and air and the perforated plate. Also the packing was refined more than the rest of the column. To avoid a longer calculation time the water distribution unit was not meshed completely. The water inlet was set directly over the tip of the water distributor.

In figure 5.2 different meshing areas can be seen. These sections are representative for the other zones in the bed shown in figure 5.2(b) and figure 5.2(c) required a finer mesh because of the small surfaces of the holes which provide the water and the air. Figure 5.2(a) shows a fine mesh at the packing around the balls. This zone is important for the mass transfer between the liquid and the gas phase. The fourth picture, figure 5.2(d), shows the mesh which was used for the rest of the column. Although the sections here shows a two dimensional mesh, a three dimensional geometry and mesh was used. In this case a cut was executed in the middle of the column to visualize the different types of the mesh.

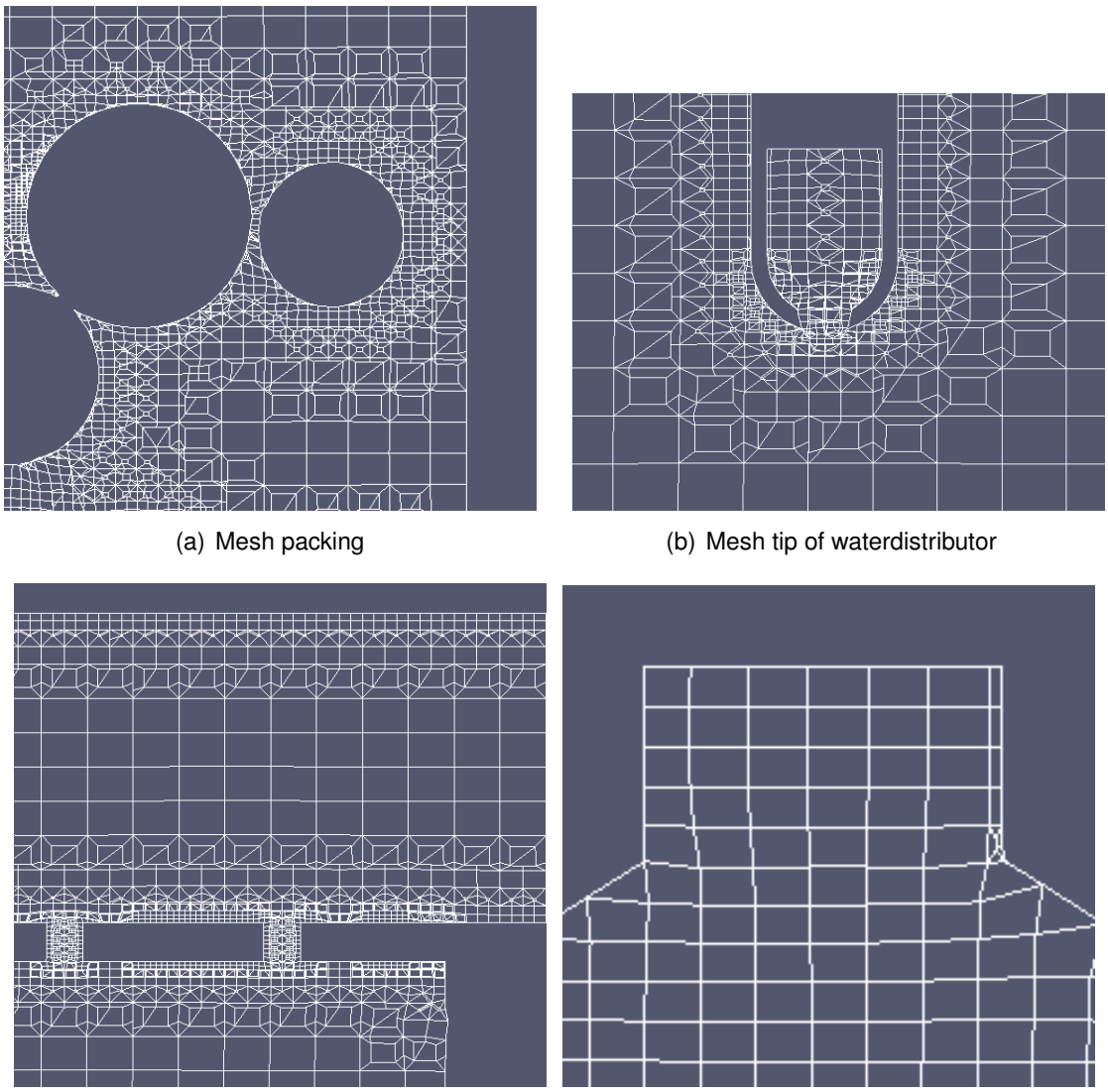

(a) Mesh packing

(b) Mesh tip of waterdistributor

(c) Mesh sparger air outlet

(d) Mesh air outlet of the column

Figure 5.2.: Different meshing details of the absorption column

5.3. Simulation

For the simulation the software OpenFOAM was used. The solver multiPhaseFoam was established by Bahram Haddadi. This solver is able to simulate multiple phases and add the mass transfer between them. The solver uses the volume of fluid (VOF) approach. The volume of fluid method describes the volumetric fraction of the phases in a defined control volume. This volumetric fraction has value one if just the first phase is present, or zero,

if nothing of this phase is in this control volume. The convective transport of the phase is described in equation 5.4. In this case C stands for the volume fraction in a specific cell.

$$\frac{\delta C}{\delta t} + u \cdot \nabla C = 0 \tag{5.4}$$

Equation 5.4 shows the transport of the volume fraction C. The flow velocity u, a velocity field, characterize the movement of C in a convective transport. The result of the moving phase are changes of the physical properties, as the density and viscosity, in the calculation areas. The new characterizing values of the phase are used for the calculation of the velocity field with the Navier-Stokes equations. The material derivative of the volume fraction C describes this approach [Hirt and Nichols, 1981].

Because of the huge number of cells and the necessary high computing power, that is needed for the VOF model it was not possible to simulate this case on the stationary server of the TU-Wien. To get higher processing power the Vienna Scientific Cluster 3 (VSC3) was used. Access was provided by the TU-Wien. The Simulation was calculated on 320 cores. The first goal of the simulation was to get a starting position for further simulations. Altough a water volume was already created via the set fields function of OpenFOAM in the sump of the column the water had to be distributed in the packed bed to create a wet surface on the packing material. Also the perforated plate had to be filled. The weir should work directly without any delay at simulations in the future. To provide a good starting point for further experiments the VSC3 calculated for 21 days. In this time approximately 23 seconds of physical real time were simulated. This shows the high computational effort for this scenario. For wetting the column a high water flow rate of 250 l/h and a low air flow rate of 19.6 m^3/h was chosen. The higher water flow rate should wet the packing in a more efficient way. The air flow was used to prevent the water from running through the perforated plate in the holes which are responsible for the air distribution.

The results from this simulation were not as expected. The appearing velocity field showed a unusual behavior above the trickle bed. Instead of an plug flow several fluxes can be detected around areas of the liquid phase which was carried out by the gas phase 5.3(a). A reason of that unusual behavior is the mesh. This mesh must be refined more in the area from the water distributor to the packing. In this area no water jet can be seen 5.3(b).

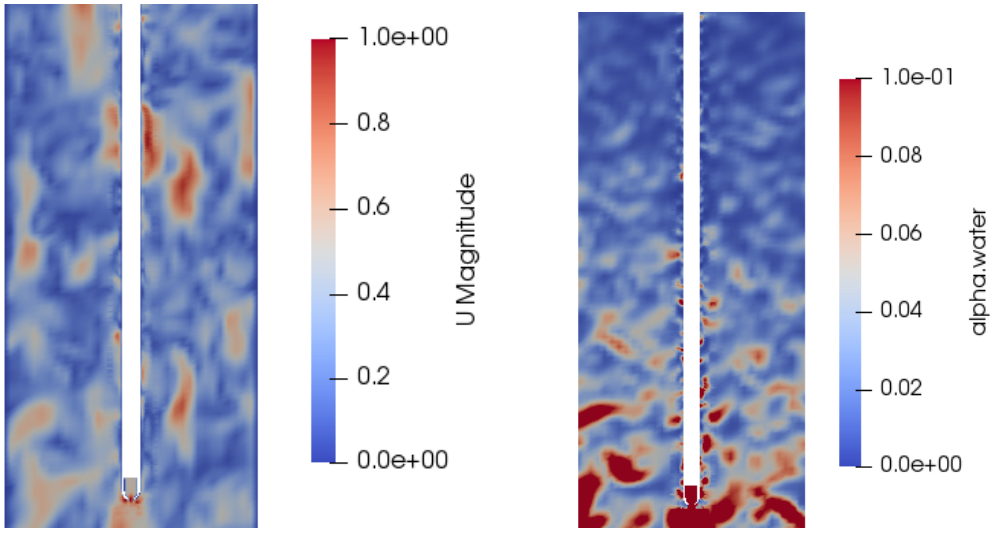

(a) Velocity magnitude above the packing (b) Amount of water above the packing

Figure 5.3.: Results of the CFD-Simulation

Creating a dynamic mesh is a proper way to handle the simulation in a different way.

5.3.1. Porosity

The packed bed was created by a DEM simulation. In this case a global porosity of 0.4 occurred (see chapter 4.2). A trickle bed does not have the same porosity on each point of the packing and the porosity behavior as seen in figure 2.14 is expected. The tool paraview was used to investigate the porosity in the simulated packing. The porosity was investigated punctual from the wall of the absorption column to the center. Because of the symmetry of the trickle bed the values for the porosity have been evaluated in one direction.

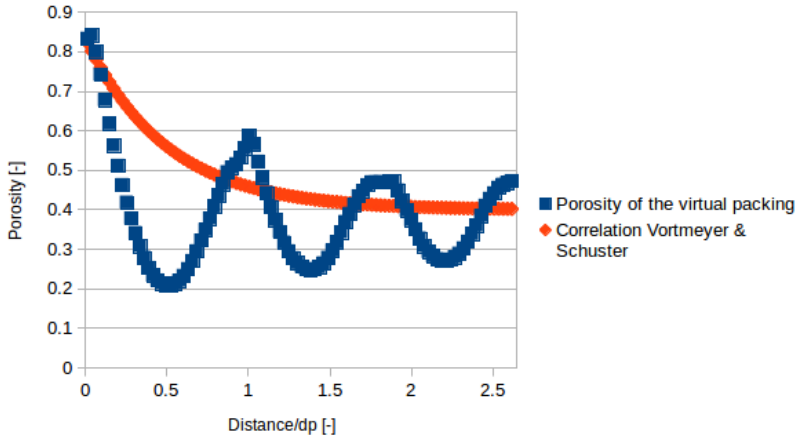

Figure 5.4.: Porosity of the packed bed

The evaluated curve (figure 5.4) of the porosity is similar to the expected behavior. Next to the wall the highest porosity occurs. The value is practically one and transient oscillating to the calculated global porosity. It can be seen that a steady porosity is not reached until the center of the column. This is because of the particle diameter. A smaller particle diameter would lead faster to the global porosity. To reach the global porosity until the center of the column a diameter of 18 mm is needed. For a nearly constant porosity distribution in the packed bed an even smaller diameter of the particle or a bigger absorption column is required.

The trend of the porosity was also compared to the equation for rectangular beds of Vortmeyer and Schuster 2.42. In figure 5.4 the function is compared to the virtual packing. The result shows a realistic behavior of the porosity for the virtual packing.

Chapter 6.

Conclusion and Outlook

The presented work summarizes the essential steps to extend an existing bubble column to be able to operate it as a trickle bed absorption reactor. The first results from the experiments on the modified setup characterize the residence time behavior of the absorption column and can be used as a valuable base for further experimental runs in the future.

To evaluate the residence time and the axial dispersion of the trickle bed, a sodium sulfate tracer solution was injected on the top of the column and the pulse response of the conductivity was recorded on the bottom of the trickle bed. The recorded data have been fitted using the distribution curve of Levenspiel. It is shown that this approach fits well for our experimental setup. The distribution function of Levenspiel delivers the possibility to calculate values for the distribution coefficient and the average residence time of the water in the packed bed. It can be seen, that the average velocity of the water threw the packing is not dependent of the gas flow rates. The backmixing of the liquid phase is described with the Bodenstein number. Two experimental runs at lower water flow rates, 100 l/h and 175 l/h, show no visible dependency of the backmixing on the air flow rate. The highest flow rate of 250 l/h shows a distinct back mixing behavior can be indentified at the higher air flow rates. The correlations of Seyed, Otake, DeMaria and White show reasonably comparable results to our experiments for all combinations of the different water and gas flow rates. The setup has also been prepared for further measurements by pre-installation of additional sensors (humidity, temperature, flow rates). The cabling for later upgrading to an automated data acquisition system (PLC or microcontroller based data logger) has also been installed, this will allow for faster and more precise experimental runs in future. For easier data evaluation it is recommended to optimize the tracer signal-to-noise ratio (e. g. by increasing the tracer

solution concentration or by using demineralized or distilled water to reduce the background conductivity).

Additional mass transfer experiments showed a no dependency of the oxygen transfer on the different flow rates of the gas- or the liquid phases in this setup. The tested flow conditions show similar amounts of transferred oxygen. To detect different oxygen transfer rates at different flow conditions, without changes on the experimental setup, the packing would have to be changed. Smaller particle would lead to a bigger surface for the oxygen transfer and a higher average residence time of the liquid phase in the packing.

In order to run CFD simulations of the experimental tests, the geometry of the trickle bed and the relevant boundaries have been implemented in CAD. The virtual packing, created by the discrete element method (DEM), shows comparable behavior to the real packing, the particle count in the computed packed bed was within 2 % of the real packing. The average porosity has small differences, which can be explained by measuring errors on the real packing. The local porosity of the virtual packing shows a similar behavior as the trickle bed in the experiment. It can also be mentioned that the approach of Vortmeyer and Schuster delivers useful results to predict the local porosity. The CFD simulation using a new invented multiphase solver showed a stable calculation for the whole period of more than 21 days, but unfortunately the simulation run could not be completed within the thesis duration. A calculation with a dynamic mesh can be considered for the future to refine explicit regions. For investigations in the future a mesh with less cells should be created to speed up the simulation.

Appendix A.

Schematics

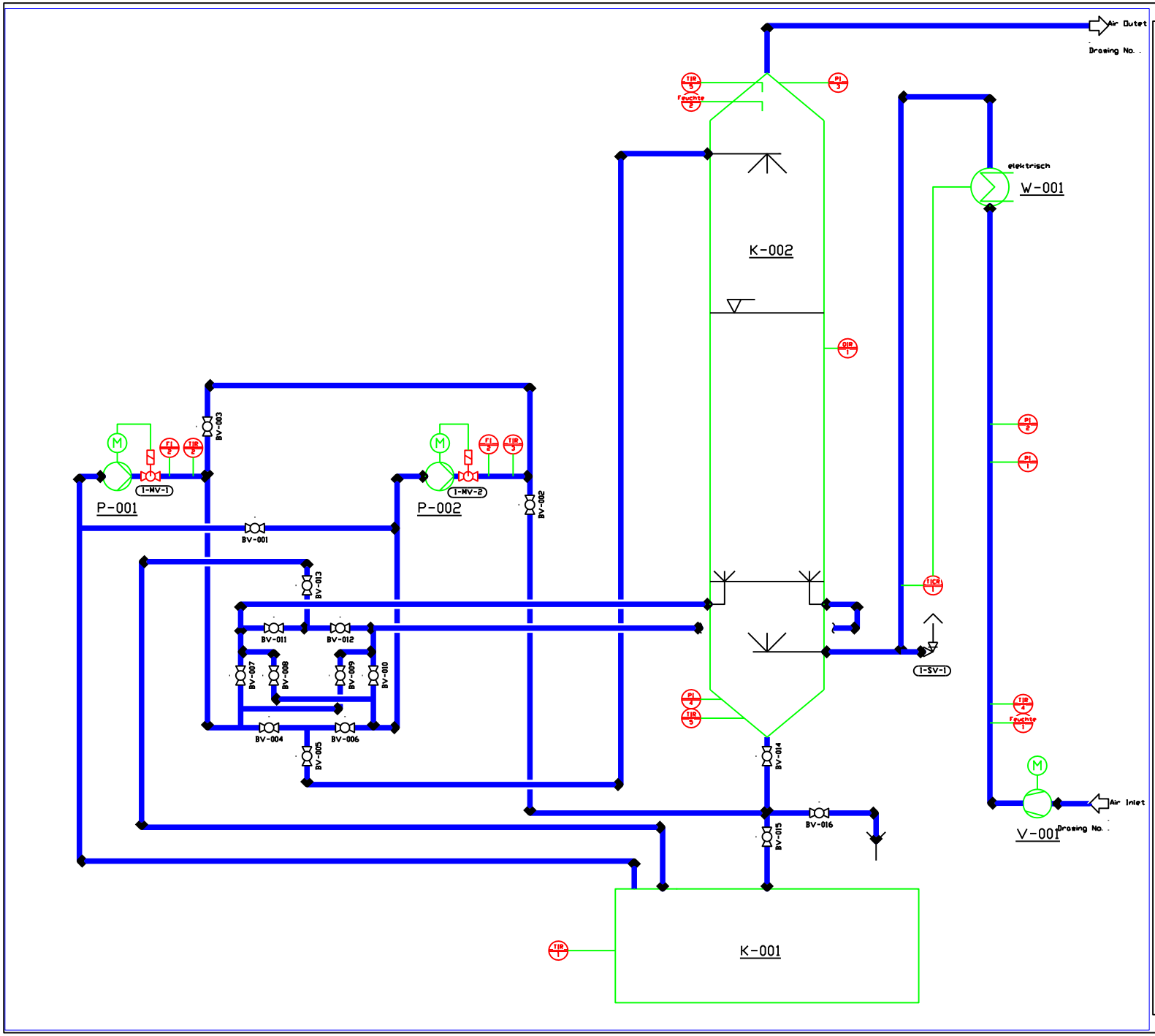

Allgemeine Anmerkungen

Nr.	Revision/Ausgabe	Datum

Zeichnungsname

Absorption Column

Projektname und -adresse

Fläche	Stempel
Zeichnungsnummer: 1	
Autor: Maximilian Reindl	

C:\Users\Max\Google Drive\Diplomarbeit\AutoCAD\BubbleColumn\PID DWG\BubbleColumn.dwg

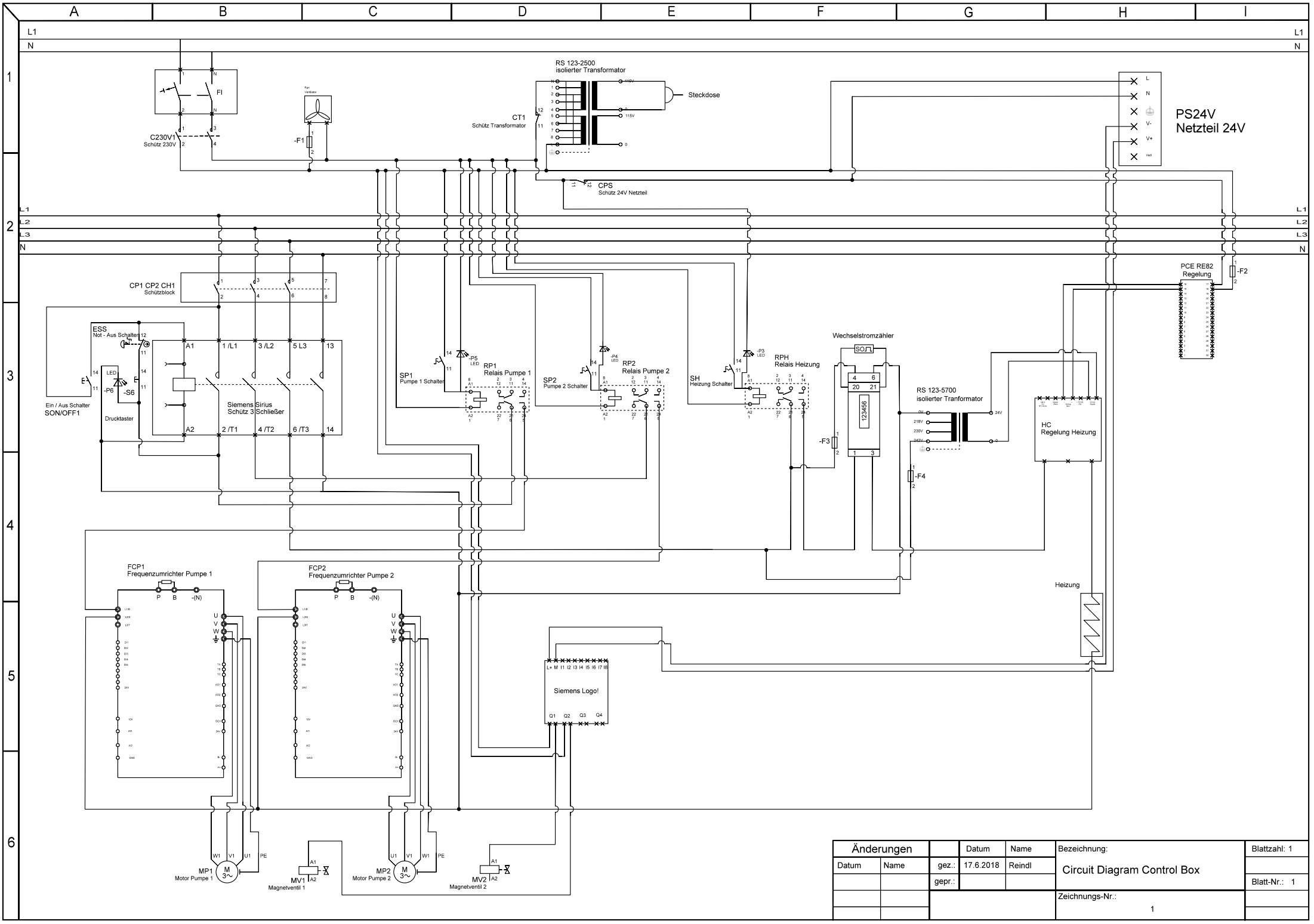

Änderungen			Datum	Name	Bezeichnung:	Blattzahl: 1
Datum	Name	gez.:	17.6.2018	Reindl	Circuit Diagram Control Box	
		gepr.:				Blatt-Nr.: 1
					Zeichnungs-Nr.: 1	

Tag	Beschreibung	Discription	Remarks
FI	FI-Schutschalter 230V	ground fault circuit interrupter 230V	protect 230 V circuit
C230V	Schütz 230V	230V contactor	protect 230 V circuit
CT	Schütz Transformator	contactor transformator	
CPS	Schütz 24V Netzteil	contactor 24V power supply	protect 24 V power supply
P230V	Steckblock Phase 230V	plug in block phase 230V	
N230V	Steckblock Null 230V	plug in block null 230V	
RS 123-2500	isolierter Transformator	isolating transformator	provide 115 V to power plug
PS24V	Netzteil 24V	power supply 24V	supply Siemens Logo!
CP1	Schütz Pumpe 1	contactor pump 1	protect pump 1
CP2	Schütz Pumpe 2	contactor pump 2	protect pump 2
CH	Schütz Heizung	contactor heater	protect heater
N400V	Steckblock Null 400V	plug in block null 400V	
Siemens Sirius	Schütz 3 Schliesser	contactor 3 turnkey	
RP1	Relais Pumpe 1	relay pump 1	switches pump 1
RP2	Relais Pumpe 2	relay pump 2	switches pump 2
RPH	Relais Heizung	relay heater	switches heater
RS 123-5700	isolierter Transformator	isolating transformer	supply heater control
PCH	Leistungsmesser Heizung	power counter heater	
HC	Regelung Heizung	heater control	
FAN	Ventilator	fan	
FCP1	Frequenzumrichter Pumpe 1	frequency converter pump 1	control pump 1
FCP2	Frequenzumrichter Pumpe 2	frequency converter pump 2	control pump 2
ESS	Not - Aus Schalter	emergency stop switch	
SH	Heizung Schalter	heater switch	
SON/OFF	Ein / Aus Schalter	on / off switch	
SP1	Pumpe 1 Schalter	pump 1 switch	
SP2	Pumpe 2 Schalter	pump 2 switch	

Table A.1.: Parts of the control box

A-A (1:1)

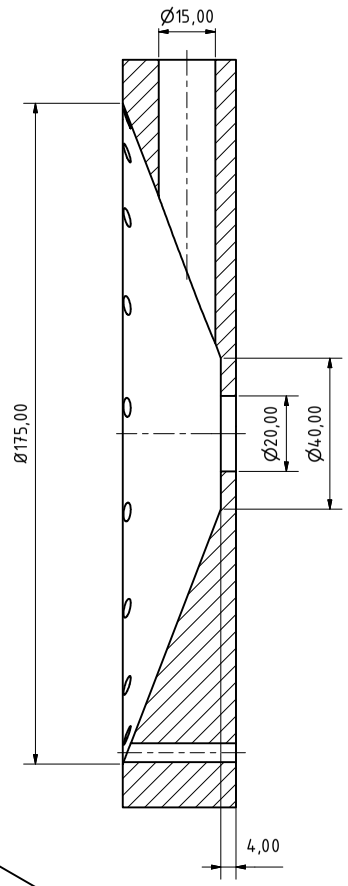

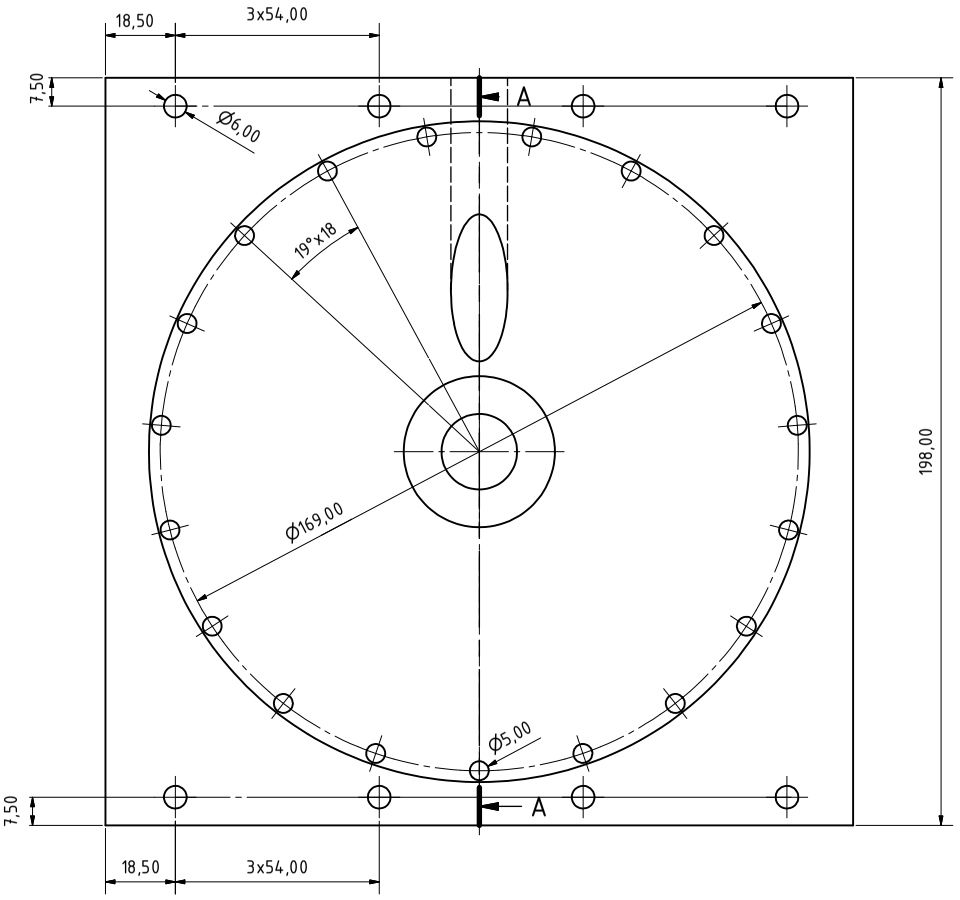

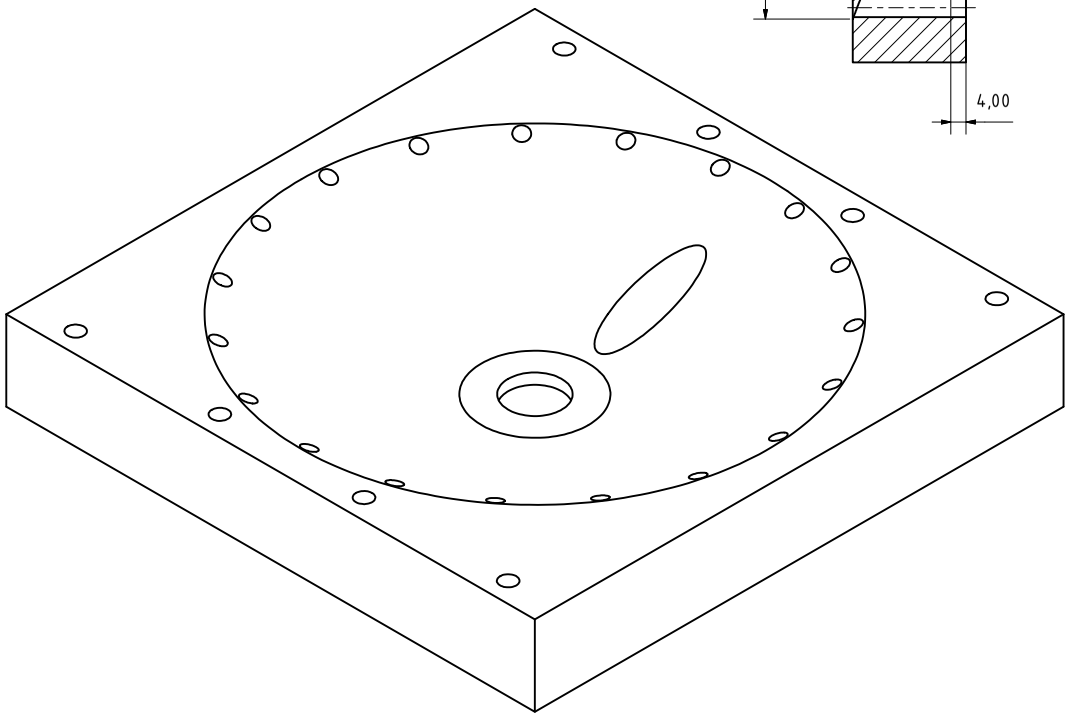

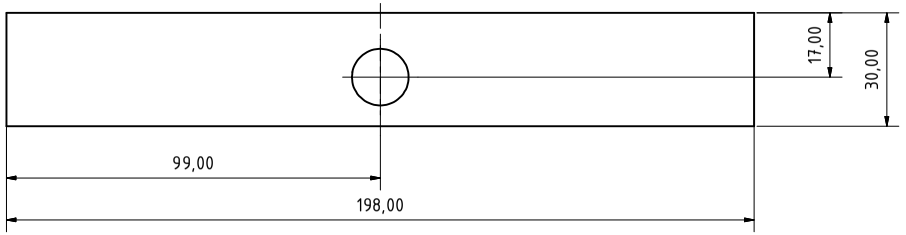

						Datum	Name	Lochplatte
					Gezeichn.	25.06.2018	Reindl	
					Kontrollt.			
					Norm			
								A2
Status	Änderungen		Datum	Name				

Appendix B.

Tables

B.1. Dissolved Oxygen Measurement

	Greisinger GMH 3630	Voltcraft DO-100
Volume fraction O_2	**dissolved O_2**	**dissolved O_2**
0	1.05	0.4
5	1.84	1.4
10	2.87	2.9
15	3.65	3.9
20	5.57	6.7
25	6.26	7.6

Table B.1.: Dissolved oxygen of 1st experiment

	Greisinger GMH 3630	Voltcraft DO-100
Volume fraction O_2	**dissolved O_2**	**dissolved O_2**
0	1.16	0.4
5	2.06	1.6
10	2.98	2.8
15	4.35	4.6
20	5.35	6
25	6.1	7

Table B.2.: Dissolved oxygen of 2nd experiment

	Greisinger GMH 3630	**Voltcraft DO-100**
Volume fraction O_2	**dissolved O_2**	**dissolved O_2**
0	1.6	0.4
5	2.2	1.3
10	3.1	2.6
15	4.08	4.1
20	5.1	5.6
25	5.9	6.7

Table B.3.: Dissolved oxygen of 3rd experiment

	Greisinger GMH 3630	**Voltcraft DO-100**
Volume fraction O_2	**dissolved O_2**	**dissolved O_2**
0	1.44	0.4
5	2.2	1.2
10	3.68	3.6
15	4.4	4.7
20	5.5	5.4
25	6.35	6.35

Table B.4.: Dissolved oxygen of 4th experiment

	Greisinger GMH 3630	**Voltcraft DO-100**
Volume fraction O_2	**dissolved O_2**	**dissolved O_2**
0	0.9	0.4
5	1.6	1.2
10	2.5	2.4
15	3.7	3.8
20	5.3	5.5
25	6	6.5

Table B.5.: Dissolved oxygen of 5th experiment

	Greisinger GMH 3630	**Voltcraft DO-100**
Volume fraction O_2	**dissolved O_2**	**dissolved O_2**
0	1.26	0.4
5	1.84	1.3
10	3.87	3.6
15	5.4	5.7
20	6.58	7
25	7.79	8.2

Table B.6.: Dissolved oxygen of 6th experiment

	Greisinger GMH 3630	**Voltcraft DO-100**
Volume fraction O_2	**dissolved O_2**	**dissolved O_2**
0	1.1	0.3
5	2.34	1.9
10	3.42	3.2
15	5.04	5.3
20	6.13	6.7
25	6.52	8.1

Table B.7.: Dissolved oxygen of 7th experiment

Appendix C.

Bibliography

[VDI, 2013] (2013). *VDI-Wärmeatlas*. VDI-Buch. Springer Berlin Heidelberg, Berlin, Heidelberg, Berlin, Heidelberg.

[Atmakidis and Kenig, 2012] Atmakidis, T. and Kenig, E. Y. (2012). Numerical analysis of mass transfer in packed-bed reactors with irregular particle arrangements. *Chemical Engineering Science*, 81:77 – 83.

[Bähr and Stephan, 2006] Bähr, H. D. and Stephan, K. (2006). *Wärme- und Stoffübertragung*. Springer, Berlin; Heidelberg; New York.

[Bird, 2007] Bird, Byron, S. (2007). *Transport phenomena*. Wiley.

[Bittante et al., 2014] Bittante, A., Garcia-Serna, J., Biasi, P., Sobron, F., and Salmi, T. (2014). Residence time and axial dispersion of liquids in trickle bed reactors at laboratory scale. *Chemical Engineering Journal*, 250:99 – 111.

[Brauer, 1971] Brauer, H. (1971). *Grundlagen der Einphasen- und Mehrphasenstroemungen*. Grundlagen der chemischen Technik. Sauerländer, Aarau [u.a.].

[Chmiel, 2011] Chmiel, H. (2011). *Bioprozesstechnik*. Spektrum Akademischer Verlag.

[Danckwerts, 1951] Danckwerts, P. (1951). Significance of liquid-film coefficients in gas absorption. *Ind. Eng. Chem.*, 43:1460 – 1467.

[Demaria and R. White, 1960] Demaria, F. and R. White, R. (1960). Transient response study of gas flowing through irrigated packing. 6:473 – 481.

[Ferziger, 2002] Ferziger, Peric, M. (2002). *Numerische Stroemungsmechanik*. Springer-Verlag Berlin Heidelberg, Berlin, Heidelberg.

[Fu and Tan, 1996] Fu, M.-S. and Tan, C.-S. (1996). Liquid holdup and axial dispersion in trickle-bed reactors. *Chemical Engineering Science, 1996, Vol.51(24), pp.5357-5361*.

[Gianetto and Specchia, 1992] Gianetto, A. and Specchia, V. (1992). Trickle-bed reactors: state of art and perspectives. *Chemical Engineering Science*, 47(13):3197 – 3213.

[Gunjal et al., 2005] Gunjal, P. R., Kashid, M. N., Ranade, V. V., and Chaudhari, R. V. (2005). Hydrodynamics of trickle-bed reactors: Experiments and cfd modeling. *Industrial & Engineering Chemistry Research*, 44(16):6278–6294.

[Higbie, 1935] Higbie, R. (1935). The rate of absorption of a pure gas into a still liquid during a short time of exposure. *Trans. Am. Inst. Chem. Eng.*, 31:365 – 389.

[Hirt and Nichols, 1981] Hirt, C. and Nichols, B. (1981). Volume of fluid (vof) method for the dynamics of free boundaries. *Journal of Computational Physics*, 39(1):201 – 225.

[Iliuta et al., 1999] Iliuta, I., Larachi, F., Grandjean, B. P., and Wild, G. (1999). Gas-liquid interfacial mass transfer in trickle-bed reactors: state-of-the-art correlations. *Chemical Engineering Science*, 54(23):5633 – 5645.

[Kemper, 2013] Kemper, J. (2013). *Kinetik und Stoffübertragung bei der reaktiven CO2-Absorption/Desorption in speziellen Amin-Blends*.

[Kraume, 2012] Kraume, M. (2012). *Transportvorgänge in der Verfahrenstechnik : Grundlagen und apparative Umsetzungen*. Springer Berlin Heidelberg, Berlin, Heidelberg.

[Levenspiel, 1999] Levenspiel (1999). *Chemical Reaction Engineering*. John Wiley and Sons.

[Levenspiel and Smith, 1957] Levenspiel, O. and Smith, W. (1957). Notes on the diffusion-type model for the longitudinal mixing of fluids in flow. *Chemical Engineering Science*, 6(4):227 – 235.

[Ligny, 1970] Ligny, C. D. (1970). The contribution of eddy diffusion and of the macroscopic mobile phase velocity profile to plate height in chromatography: A literature investigation. *Journal of Chromatography A*, 49:393 – 401.

[Lohninger, 2013] Lohninger, H. (2013). Natriumsulfat (glaubersalz).

[Lukasser, 2008] Lukasser, M. (2008). *Entwicklung einer Laborblasensäule und eine Parameterstudie am Eulerschen Modell für Blasenstroemungen mit gleichmässiger Begasung*.

[Luo et al., 2014] Luo, Y., Yang, H., Lu, L., and Qi, R. (2014). A review of the mathematical models for predicting the heat and mass transfer process in the liquid desiccant dehumidifier. *Renewable and Sustainable Energy Reviews*, 31:587 – 599.

[Ohle, 2009] Ohle, A. (2009). *CO2-Abtrennung aus Gasströmen durch Absorption in Poly(methyldiglykol)amin*.

[ONDA et al., 1968] ONDA, K., TAKEUCHI, H., and OKUMOTO, Y. (1968). Mass transfer coefficients between gas and liquid phases in packed columns. *Journal of Chemical Engineering of Japan*, 1(1):56–62.

[Orgill et al., 2013] Orgill, J. J., Atiyeh, H. K., Devarapalli, M., Phillips, J. R., Lewis, R. S., and Huhnke, R. L. (2013). A comparison of mass transfer coefficients between trickle-bed, hollow fiber membrane and stirred tank reactors. *Bioresource Technology*, 133:340 – 346.

[Otake et al., 1962] Otake, T., Kunugita, E., and Yamanishi, T. (1962). Mixing characteristics of gas and liquid flowing through gas-liquid packed beds. *Chemical engineering*, 26(7):800–806.

[Potnis and Lenz, 1996] Potnis, S. and Lenz, T. (1996). Dimensionless mass-transfer correlations for packed-bed liquid-desiccant contactors. *Industrial and Engineering Chemistry Research*, 35(11).

[Prieler, 2012] Prieler, R. (2012). *Optimierung der Hydrodynamik in einer RDC-Kolonne*.

[Ram, 1966] Ram, T. K. (1966). *Axial Dispersion of liquid in packed beds*.

[Ramachandran and Chaudhari, 1983] Ramachandran, P. and Chaudhari, R. (1983). *Three-phase catalytic reactors*. Topics in chemical engineering. Gordon and Breach Science Publishers.

[Saez et al., 1991] Saez, A. E., Yepez, M. M., Cabrera, C., and Soria, E. M. (1991). Static liquid holdup in packed beds of spherical particles. *AIChE Journal*, 37(11):1733–1736.

[Seyed and Tingyue, 2017] Seyed, O. R. and Tingyue, G. (2017). Empirical correlations for axial dispersion coefficient and peclet number in fixed-bed columns. *Journal of Chromatography A*, 1490:133 – 137. Special section: Editors' Choice XI.

[Spurk and Aksel, 2007] Spurk, J. H. and Aksel, N. (2007). *Strömungslehre : Einführung in die Theorie der Strömungen*. Springer-Lehrbuch. Springer-Verlag Berlin Heidelberg, Berlin, Heidelberg, 7. auflage. edition.

[Vortmeyer and Schuster, 1983] Vortmeyer, D. and Schuster, J. (1983). Evaluation of steady flow profiles in rectangular and circular packed beds by a variational method. *Chemical Engineering Science*, 38(10):1691 – 1699.

[Yaici W., 1985] Yaici W., Laurent A., M. (1985). Determination des coefficients de transfert de matiere en phase gazeuse dans un reacteur catalytique a lit fixe arrose en presence de phases liquides aqueuses et organiques. *Bulletom de la Societe Chimique de France*.

[Zeiser, 2008] Zeiser, T. (2008). *Simulation und Analyse von durchströmten Kugelschüttungen in engen Rohren unter Verwendung von Hochleistungsrechnern*.